Structures and backscattering characteristics of CUSAT 205 MHz Stratosphere-Troposphere Radar at Cochin (10.04°N, 76.3°E) - First results

Nabarun Poddar[1,2], Siddarth Shankar Das[1,*], Veenus Venugopal[1,2], S. Abhilash[3] , V. Rakesh[3]

[1]Space Physics Laboratory, Vikram Sarabhai Space Centre, Thiruvananthapuram-695022

[2]Department of Physics, University of Kerala, Thiruvananthapuram

[3]Advanced Centre for Atmospheric Radar Research, Cochin University of Science and Technology, Cochin

e-mail: dassiddhu@yahoo.com & siddarth_das@vssc.gov.in

Abstract. This paper presents the first ever observations on aspect-sensitive characteristics of 205 MHz Stratosphere-troposphere radar located at a tropical station Cochin (10.04°N, 76.3°E) using volume scanning. The most significant and new observation is that the signal-to-noise ratio in zenith and off-zenith beams are nearly equal in some height region, indicating the presence of isotropic turbulence. Signal strength decreases by 0.75 dB per degree from 0 to 10 degree off-zenith, 0.9 dB per degree from 10 to 20 degree off-zenith and 0.3 dB per degree beyond 20 degree off-zenith. Different causative mechanisms are discussed on the basis of various estimated parameters associated with aspect sensitivity. Maximum aspect sensitivity is observed between 12 and 17 km, indicating the presence of dynamic instability arising due to strong wind shear and atmospheric stability. When both the square of wind shear and stability parameters are above 0.25×10^{-3} s^{-2}, the scatterers become mostly isotropic. The study also shows a power difference in the symmetric beams as well as azimuth angle dependency. Analysis suggests that this asymmetry is due to the tilting of layers by the action of atmospheric gravity waves generated through Kelvin-Helmholtz-instability. The

present configuration of radar can provide a better understanding of three-dimensional structures of turbulence and instabilities.

[**Keywords:** ST radar, aspect-sensitivity, Kelvin-Helmholtz-instability]

Plain language summary

Radar backscatter from the atmosphere depends directly on the turbulent scale sizes present and the probing frequency. When the backscatter echo strength decays with the radar viewing zenith angle, the signals are said to be aspect sensitive i.e., dependent on the viewing angle. There can be few circumstances under which such characteristics are observed, all primarily being anisotropic scattering processes which are caused due to various processes in the atmosphere. Such aspect sensitivity must be quantified for realising the accurate operation of a radar which would otherwise result in underestimation of winds and other parameters obtained from the radar. Here the aspect sensitivity characteristics of the 205 MHz stratosphere–troposphere (ST) radar installed at Cochin (10.04˚N, 76.33˚E) are studied using a detailed experiment using various probing techniques during Indian Summer Monsoon season and the characteristics of the atmosphere during that period are probed to explain the aspect sensitivity.

1. Introduction

A backscatter echo power and its characteristics are strongly controlled by the nature of the scatterers present in the atmosphere. A very-high frequency (VHF) radar echoes are known to be aspect sensitive in general owing to either thin stable layer providing sharp refractive index gradient or shear driven steep layer structures. The main mechanisms are isotropic and anisotropic turbulence and Fresnel reflection/scattering (e.g., Hocking et al., 1986, 1990; Jain et al., 1997; Das et al., 2008). Unlike isotropic scattering, anisotropic scattering mechanisms lead to a deterioration of the signal with increasing off-zenith angle, thus rendering the echoes 'aspect sensitive' (Röttger and Liu, 1978; Jain et al., 1997). Such aspect sensitivity effectively alters the radar parameters such as beam pointing angle and hence the quantities derived from them i.e., underestimation of the horizontal wind (Hocking et al.,1990; Damle et al., 1994; Das et al., 2022). Thus, the study of the aspect of sensitivity of such VHF radars is of utmost importance given their use as powerful tools in deciphering winds and turbulence parameters from clear air and during disturbed conditions.

Earlier studies have shown that aspect sensitivity of backscatter echoes can be linked to the presence of a thin stable layer which is effectively a single sharp gradient in radio refractive index or to the presence of shear-generated steep layer structures (Hocking et al., 1986, 1990; Tsuda et al., 1997a, Das et al.,2008, 2022). A strong thermal gradient in the vicinity of tropical tropopause (16-18 km) acts like a perfect reflector causing high aspect sensitive VHF radar echoes (Jain et al., 1997; Das et al., 2008, 2016, 2022). Quantitatively a rapid decrease of signal strength at an average of about 1.2 dB per degree till 10˚ tilt and at 0.6 dB per degree beyond that (Tsuda et al.,1997a; Anandan et al.,2008; Das et al., 2022) are attributed to Fresnel reflection/scattering and anisotropic turbulence up to 10˚ (Gage and Balsley, 1980) and those beyond 10˚ are attributed to

Bragg scale isotropic turbulent scattering (Rao et al., 1997) as observed for 49-53 MHz VHF radars. While previous studies focused mostly only on the orthogonal north-south, east-west variation of the echo strength (Damle et al., 1994; Jain et al., 1997; Qing et al., 2018; Ghosh et al., 2004; Das et al., 2008, 2016) due to the limitation of experiments, others have found an azimuthal dependence too (Tsuda et al., 1997b; Worthington et al., 1999; Das et al., 2022). The angular variation of the echo strength has been attributed to either diffuse reflection from stable temperature sheet structure or the presence of corrugated sheets or anisotropic turbulence (Das et al., 2014). Azimuth angle variation has been attributed to the presence of tilting layers which are generated due to gravity waves (Tsuda et al., 1997b; Rao et al., 2008) or mountain waves (Worthington 1999). Studies in these tilting layers have found small-scale Kelvin-Helmholtz instability (KHI) to be responsible for the redistribution of scatterers into a tilted layer (Worthington et al., 1997; Ghosh et al., 2004; Das et al., 2008, 2016). Primarily KHI is found to be in cores of large wind shears like above and below the jet stream or is created due to inertia gravity waves (IGW). Studies have found that in the UTLS region, only a minimal amount of shear is needed to generate aspect-sensitive echoes (Ghosh et al., 2004). It has also been found that all zenith beam echo powers remain the same for well mixed i.e., isotropic turbulent layers. Previous volume imaging experiment of VHF aspect sensitive scatterers have shown tilted layers (Worthington, 2005). Thus, an understanding of the causative mechanisms for aspect sensitivity has been found in the above-mentioned atmospheric processes. But two salient points from the aforementioned studies are firstly that very few of these have been done to understand the total spatial dependence of aspect sensitivity i.e., both in the off-zenith and azimuthal directions mostly due to the limitation of radar scanning patterns and most of the studies have been performed in the higher and

mid-latitudes with only a handful of them being in the tropical low latitude belt, of which most are limited to the 53 MHz radar at Gadanki (Das et al., 2022).

In this study, a state-of-the-art, indigenously developed, and the world's first stratosphere–troposphere (ST) radar operating at 205 MHz at Cochin University of Science and Technology (CUSAT), Cochin (10.04°N, 76.33°E) (Samson et al., 2016; Mohanakumar et al., 2017) has been used. This radar has a 360-degree azimuthal beam steering capability which can provide full three-dimensional atmospheric dynamics and structure in both clear-air and in extreme weather conditions. There is no aspect sensitivity study so far using a 205 MHz atmospheric radar at any other place in the world. Here, the first results obtained from the experiments conducted during clear-air and disturbed weather conditions by operating CUSAT ST-Radar in multi-beam mode with azimuthal steering are presented. The experiments were designed by the optimum selection of zenith and azimuth beams, which will have a full-volume imaging scan within ~18 min. It is envisaged that the present experiment and results will have an important aspect in designing various experiments with CUSAT- ST radar, which is located at the gate-way of the Indian Summer Monsoon (ISM) region to better understand the dynamical processes taking place in the UTLS region in terms of radar scattering mechanism. Section 2 provides the experiment details with data analysis, background meteorological conditions in section 3, results and discussion in section 4 followed by concluding remarks in section 5.

2. Experiment and Data Analysis

2.1. CUSAT ST Radar

The CUSAT ST radar is unique in the sense that it uses the 205 MHz VHF frequency. It is a pulsed coherent Doppler radar with peak power aperture product of about 1.6 x 10^8 W m^2 and 619 element antenna active phased array arranged on a rooftop in a

circular array of about 27 m diameter with an inter element spacing of 0.7 λ. The radar beam can tilt up to a maximum of 30° in the off-zenith direction and cover 0°-360° in the azimuthal direction with a step interval of 1° (Samson et al., 2016; Mohanakumar et al., 2017). Detailed radar specifications are listed in Table 1.

The experiments were performed on July 21 and 22, 2022, which is in the active phase of the Indian Summer Monsoon (ISM) season. The Radar has been operated in four modes: viz. mode-1, mode-2, mode-3, and mode-4. Here mode-1 is the 5-beam configuration operation that is used to derive the wind components from the radar, and mode-2 is the continuous vertical observation. Mode-3 is the multibeam mode operated to study the orthogonal characteristics in the east-west and north-south directions with 61 beams up to 30° angle in steps of 2°. Mode-4 is the volume scan mode using 31 beams in a scan cycle time of about 18 minutes, where the zenith and azimuthal variations are studied. Details of beam configuration and scans are given in Table 2 and the corresponding beam configuration in space for modes 1,2, 3, and 4 are shown in Figure 1. The radar data is recorded in terms of I (in-phase) and Q (quadrature) values for each beam position of the scan which is processed by algorithms to read these values from the raw binary format file to produce the power spectrum and this has been utilized to derive the moments that have been essentially used in this work to further derive the wind and turbulence parameters using a multibeam technique to minimize errors.

2.2. Radiosonde

Regular GPS-based radiosonde (Chang Feng CF-06-A make) are launched at India Meteorological Department (IMD) from Cochin and Thiruvananthapuram (8.48°N, 76.95°E) at 05:30 and 17:30 LT. But on the day of experiment, we have radiosonde observation from Thiruvananthapuram only. These radiosondes have an accuracy of better than 2 ms^{-1} in wind velocity. The profiles obtained from radiosonde

150 measurements are interpolated into 100 m resolution. The soundings were obtained
151 from the University of Wyoming sounding data archive
152 (http://weather.uwyo.edu/upperair/sounding.html).

153 **2.3. Satellite observations**

154 The Constellation Observing System for Meteorology, Ionosphere, and Climate-2
155 (COSMIC-2) satellite constellation gives excellent profiles of the atmosphere temperature
156 and humidity by using the GPS Radio Occultation (RO) technique and has very good
157 temporal and spatial coverage over the tropical region (Veenus et al., 2022). The absolute
158 temperature difference between COSMIC-2 measured temperature with radiosonde
159 observation is about 0.5 K and a standard deviation difference of 1.5 K. Hence the closest
160 temporal and spatial occulted temperature profile obtained from COSMIC-2 has been
161 utilized in the present study. In addition, the outgoing long-wave radiation (OLR)
162 obtained from the imager aboard the geostationary Indian meteorological satellite
163 (INSAT)-3DR, gives an indicator of intensity of convection.

164 **2.3. IMDAA reanalysis**

165 The Indian Monsoon Data Assimilation and Analysis (IMDAA) reanalysis is a high-
166 resolution reanalysis data over the Indian Summer Monsoon (ISM) region developed by
167 the Ministry of Earth Sciences (MoES), Government of India with the collaboration of Met
168 Office, UK under the Indian Monsoon Mission project (Ashrit et al., 2020; Rani et al.,
169 2021). The data assimilation scheme in IMDAA reanalysis used is 4D-Var (four-
170 dimensional variational) of the upper-air atmospheric state and has assimilated both
171 satellite and in situ observations and it's a unified model. The horizontal grid resolution
172 is ~12 km and it has 63 vertical levels up to 40 km. Details can be found elsewhere (Ashrit
173 et al., 2020; Rani et al., 2021). We also used winds and mean sea level pressure from
174 IMDAA reanalysis.

3. Meteorological background

The experiments were conducted during the active phase of tropical easterly jet (TEJ). Figure 2 (a) shows the intensity of wind speed and direction at 100 hPa at 13:30 LT on July 21 and 22, 2022. Wind speed and direction are obtained from IMDAA reanalysis. It is clear from the figure that the core of TEJ is located over the radar observational site. There is a variation of the core size and shape from July 21 to 22, 2022. As outgoing-long wave radiation (OLR) is considered as the proxy of convection, thus we have plotted OLR obtained from INSAT-3DR on both the days as shown in Figure 2 (b). On July 21, 2022, a clear sky is observed over the radar site, however, intense clouds were observed over the north Indian Ocean. In contradictory, we observed clouds on July 22, 2022 over the radar site as well as over the central India and North Bay of Bengal. As such no low pressure systems were observed on both days (Figure 2 b).

4 Results and Discussion

4.1 Fan Sector and Volume scan

Figure 3a shows the fan sector variation of signal-to-noise ratio (SNR) in East-West (EW) and North-South (NS) extending to a horizontal maximum of about 10 km on either side of the zenith beam using mode-3 experiment at 13:30 LT on July 22, 2022. Enhancement of the SNR across the horizontal direction at ~17 km in both the EW and NS fan sectors is seen in the vicinity of tropopause (VOT). Aspect-sensitive characteristics are clearly evident above ~12 km in both the SNR plots and it is observed that SNR decreases with an increase in off-zenith angles. A similar variation of SNR has earlier been reported in those height ranges for the 53 MHz Gadanki MST radar (Jain et al., 1997; Ghosh et al., 2004; Das et al., 2008, 2016) during both clear and disturbed weather conditions. Similarly, a fan sector study of the beam line-of-sight Doppler velocity gives an idea about the dynamics as seen in Figure 3b where a stark difference is noted in the

strength and characteristics of the Doppler values from EW and NS fan sectors. The strong easterly Doppler was observed as a Tropical Easterly Jet (TEJ) above 12 km which is a feature related to the ISM. On the contrary, the NS Doppler has asymmetric features although not as strong as the EW Doppler. Figure 3c shows the fan sector map of the uncorrected half-power full spectral width which is quite similar in feature to the SNR. Enhancements in spectral width corresponding to areas of enhanced SNR are observed, which indicates the presence of turbulence. This spectral width can be contaminated with non-turbulent factors like broadening due to the finite volume of the beam, shear broadening, and transient effects, which will be discussed later. Similar features can also be noted for July 21, 2022 as shown in supplementary Figure S1.

Figure 4 shows the SNR variation with zenith angles up to 30˚ in the EW and NS planes for different heights during mode-3 experiment on July 22, 2022. It can be seen at 11.4 km that the SNR falls very gradually with increasing off-zenith angle remaining almost same up to ~6˚ on either side of the zenith beam in both EW and NS directions showing isotropy in that region. Similar feature can be noted for 12.4 km too but only in the EW direction as NS plane shows regularly decreasing SNR feature with increasing off-zenith angle. Such EW and NS plane asymmetry is noted at 14 km and 16.4 km too as shown along with significant off-zenith enhancement of SNR which can be attributed to tilted scatterer layer perpendicular to the beam direction (Muschinski and Wode, 1998). For July 21, 2022 such variation of SNR is also observed with similar EW and NS asymmetry as shown in Figure S2.

After averaging all fan scans for both EW and NS directions respectively heights with least isotropy, off-zenith asymmetry and off-zenith enhancement are found out. From such heights with progressively decaying signal, it is estimated that the signal strength decreases by 0.75 dB per degree from 0 to 10 degree off-zenith, 0.9 dB per

degree from 10 to 20 degree off-zenith and 0.3 dB per degree beyond 20 degree off-zenith using the formula:

$$Decay = \frac{SNR_{\theta_a} - SNR_{\theta_b}}{\theta_a - \theta_b} \quad (1)$$

where θ_a takes values 0°,10°, 20° and θ_b takes values 10°,20°, 30° respectively.

It is observed from Figure 5 that Doppler frequency spectra as a function of zenith angle for both EW and NS plane scans are mostly narrow for both the panels especially for lesser zenith angles, showing smaller spectral widths between 13:01:36-14:46:00 LT on July 22, 2022. The slope of the mean spectra indicates and validates the presence of background wind in both the orthogonal planes, a feature previously observed by Das et al. (2008) for a different location. Notably, much higher range of Doppler values are seen in EW panel owing to the strong Doppler associated with the TEJ as shown earlier. Weaker echoes for higher Doppler values at large zenith angles are consistent with the fan sector plot for the same. Further Figure S3 shows almost exactly the same features on July 21, 2022 during the time span.

Figure 6 shows the slice maps of the radar scan volume which provide the spatial variation of SNR, Doppler, and spectral width at different height levels at 12 LT on July 22, 2022. It is to be noted that above 14 km the SNR shows a general aspect sensitivity with echo strengths decreasing towards the edge of the volume slices but with a very evident asymmetry in the azimuthal direction for all three heights. Isotropic scattering is observed at ~17.6 km, which is the tropopause level as observed from the temperature profile. In the VOT level, the volume slice shows very regular high SNR spread around the zenith region signifying a stratified layer. While much stronger asymmetry of signal is noted at 14 km with strong off-zenith enhancement. This feature as explained earlier may be attributed to the presence of tilting layers. Symmetric Doppler feature is observed in

Figure 6b. The spectral width slice maps shown in Figure 6c represent the spatial distribution of turbulence. Volume slices for July 21, 2022 are shown in Figure S4.

4.2 Aspect sensitivity mechanisms and characteristics

Aspect sensitivity as mentioned before can be understood by the relative strength of the zenith beam echo with respect to the off-zenith echoes as shown in Figure 7. It can clearly be seen that the deviation of SNR from the zenith value is more prevalent above the heights of ~12 km for the angles shown for east, west, north, and south directions. In all the directions, a decrease in the difference below zero in between 14-16 km heights and an increasing trend above 16 km for higher off-zenith angles is observed. From such distribution of SNR, it can be said that for layers below 10-12 km, the echo strengths are more or less the same for most off-zenith angles due to isotropic turbulent scatter. While a positive zenith-off-zenith SNR difference can be attributed to the presence of stratified layer, a negative difference for the same as noted between ~14-15 km can possibly be due to the tilting layers associated with gravity waves or KHI, which will be discussed. Figure S5 shows similar features but for July 21, 2022.

Aspect sensitivity parameters can be characterized by the aspect angle (θ_s) which is the measure of anisotropy and can be derived from the backscatter echo powers for one zenith angle with respect to another (Hocking 1986; Hocking 1989) as shown in equation (2):

$$\theta_S = sin^{-1}\sqrt{\frac{sin^2\theta_{b_2} - sin^2\theta_{b_1}}{ln\left({P(\theta_{b_1})}/{P(\theta_{b_2})}\right)} - sin^2\theta_0} \quad (2)$$

where θ_0 (=$\theta_{3\ dB}/\sqrt{ln\,2}$), the e^{-1} half-width of the radar polar diagram, is 1.8° for a $\theta_{3\ dB}$ (3-dB beam width) of 3° in the CUSAT ST radar. θ_b is the zenith or beam pointing angle. Aspect angle is calculated with respect to the zenith beam here thus, $\theta_{b_1} = 0^\circ$. Another parameter is the corresponding horizontal correlation length (ζ) (length-to-depth ratio)

of the scatterers in the atmosphere which is obtained (Hocking et al 1990) by equation (3):

$$\zeta = \frac{15.2\lambda}{\theta_S} \quad (3)$$

Corresponding values of θ_s and ζ for different off-zenith beam angles with respect to the zenith beam for all the four orthogonal directions *viz*., east, west, north, and south on July 22, 2022 as shown in Figure 8. To understand the significance of Fresnel scattering/ reflection the condition $\zeta \geq 0.29D$ (D is diameter of the antenna) (Gage 1990) must hold. In this case accounting for the geometry of the radar $\zeta \geq 7.187$ m and correspondingly $\theta_S \leq 3.093^{\circ}$ give the Fresnel scattering threshold. Figure 8 shows lower values of aspect angle for lesser zenith angles and corresponding higher correlation length above 14 km height for all four directions (E,W,N,S) with slight variations. This implies the presence of anisotropic scattering mechanisms such as Fresnel scattering or anisotropic turbulence. Values of θ_s and ζ occurring below and above the thresholds marked respectively are seen only in layers between 12-17 km, signifying Fresnel scattering/reflection. Some differences in pattern in the EW and NS directions especially in the lower heights below 12 km show the azimuthal asymmetry of aspect sensitivity. Similar distribution of aspect angle and correlation length on July 21, 2022 can be seen in Figure S6.

The anisotropy estimated above affects the actual beam pointing angle at different heights, but from the measure of θ_s the effective beam pointing angle can be calculated as:

$$sin(\theta_{eff}) = sin(\theta_b)\left(1 + \frac{sin^2\theta_0}{sin^2\theta_s}\right)^{-1} \quad (4)$$

This is the source of underestimation of winds using the radar. Figure 9 shows the effective beam pointing angle for zenith angles up to 16° on July 22, 2022. Deviation from the original beam pointing angle is clearly visible above 12 km with very large deviation

297 at and above 14 km up to ~16 km height for all zenith beam in all the four orthogonal
298 directions. Interestingly, it is to be noted that for angles less than 6˚ the deviation from
299 the true pointing angle is more as compared to angles above 6˚, this leads to the
300 significant underestimation of wind when using such low zenith angles. Almost same
301 trend is also observed for July 21, 2022 as shown in Figure S7 but with significantly higher
302 deviations for lower angles up to 8 ˚. Thus, knowing the effective beam pointing angle
303 leads to a quantitative measure of the underestimation of wind components at different
304 heights.

305 **4.3 Dependency of aspect sensitivity on wind shear and atmospheric stability**

306 Both the atmospheric stability and vertical shear play a major role in the aspect
307 sensitivity of VHF radar (e.g., Ghosh et al., 2004; Das et al., 2022). Thus, we estimate the
308 atmospheric stability (N^2) using equation (5):

309 $$N^2 = \frac{g}{\theta}\left(\frac{\partial\theta}{\partial z}\right) \quad (5)$$

310 where, N is the Brunt-Vaisala frequency, θ the potential temperature, which is estimated
311 from the temperature profile obtained from COSMIC-2 GPS RO. Further, vertical shear of
312 horizontal wind (S^2) is estimated using equation (6):

313 $$S^2 = \left(\frac{\partial u}{\partial z}\right)^2 + \left(\frac{\partial v}{\partial z}\right)^2 \quad (6)$$

314 Where, u and v are the CUSAT ST radar derived velocity of zonal and meridional wind,
315 respectively. Figure 10 shows a variation of difference of SNR with respect to the zenith
316 beam with square of (a) wind shear (b) stability parameters for July 22, 2022. It is clearly
317 evident from both the top (EW) and bottom (NS) panels of Figure 10a that the probability
318 of having high aspect sensitivity is enhanced when S^2 is less than 0.25×10^{-3} s^{-2} , shown as
319 a denser cluster of points. Beyond this threshold it can be said that the increased shear
320 causes turbulent mixing resulting in isotropy of the scatterers. Shear also does play an

important role of resharpening of refractive index gradient as pointed out and explained by Muschinski and Wode (1998). Similarly in Figure 10b for the case of N^2 the same characteristics can be seen where with a dense cluster of points inside the $0.25x10^{-3}$ s^{-2} threshold limit albeit not as strongly defined as the shear parameter. But it can be concluded that beyond the stability threshold the scatterers become isotropic. The exact same feature is also reproduced for July 21, 2022 as seen in Figure S8. Previous study by Das et al. (2022) showed similar results for the Gadanki MST radar at 53 MHz.

4.3 Role of Kelvin-Helmholtz Instability and gravity waves in tilting layer

The preceding analyses throw light on the spatial aspect sensitivity characteristics but to understand the temporal evolution of the backscatter echoes, the CUSAT ST radar was operated in mode-2, i.e., continuous vertical observations made from 14:10 to 16:10 LT on July 22, 2022. Figure 11 shows the height-time-intensity (HTI) plots of (a) SNR, (b) vertical velocity, and (c) half-power full spectral width. Enhanced SNR layer is seen in the VOT similar to the fan sector plots in Figure 11a. Aspect sensitivity is very clearly observed around and above 12 km. An enhanced SNR structure is seen at around 14 km height with a descending trend with time from 15:30 LT onwards. The corresponding HTI plot of vertical velocity in Figure 11b obtained from the line- of-sight Doppler ($w = -\lambda/_2\, d$) shows alternating upward and downward velocities at ~14 km after 15:30 LT. This resembles a turning structure which can be attributed to KHI. Such a pronounced alternating episode of updraft and downdraft is not seen anywhere else in the HTI plot but a feature of note is the presence of strong updrafts above 14 km height for the given time period owing to the convective conditions on the day most notably above the KHI structure in the VOT. Strong descending downdraft structures are seen below 10 km after the strong KHI signature. In Figure 11c uncorrected half power full spectral width shows enhanced turbulence corresponding to high spectral width mostly below 12 km height

346 temporally corresponding to the KHI and the descending downdraft structure.
347 Enhancement of spectral width can be seen just below the tropopause all through and
348 around 14 km height post 15:30 LT matching with the SNR feature in Figure 11a. The
349 observed features mentioned above are quantified by studying the stability, wind shear,
350 as shown in Figure 12 for July 22, 2022. COSMIC-2 temperature profile and wind speed
351 components obtained from the radar. It has been found that the cold point tropopause
352 (CPT) lies at about 17.6 km for this time of observation and a huge increase in the stability
353 and decrease in wind shear at that level is seen in Figures 12c and 12d. Comparing all the
354 heights it can be said from previous studies (Ghosh et al., 2004) that a sharp gradient
355 instability and reduction of wind shear indicates aspect sensitivity thus showing that
356 aspect sensitivity is dependent on the thermal structure of the atmosphere. Figure 12e
357 shows the corresponding Richardson Number ($Ri=N^2/S^2$) profile which gives a measure
358 of turbulence. Values less than 1 suggest turbulent layers and more than 1 suggest aspect-
359 sensitive regions. A sharp reduction in Richardson number to under the threshold value
360 at around 14 km explains the turbulent feature observed in Figure 11. While aspect
361 sensitive layers do not occur much up to 10 km as observed, these become more
362 prevalent above 12 km height except for the height range of around 16 km. This height
363 range corresponds to the TEJ core as seen in Figure 12a and this feature also matches
364 with the wind profile derived from radiosonde observation for the day. The tropopause
365 being a stably stratified layer shows maximum stability, minimum shear, and an
366 extremely high value of Richardson number, indicating the presence of KHI. Similar
367 features are noted for July 21, 2022 as shown in Figure S9.
368 The asymmetry in SNR (Fig.7 and Fig. S5) can be due to this observed KHI,
369 however gravity waves can also contribute for titling layer. To get further insight, the
370 time-series of vertical velocity is subjected to Fast-Fourier transform (FFT) to obtain the

gravity wave spectra. Figure 13 shows the (a) power spectra of vertical velocity at 14.8 and 15.7 km. The dominant period of gravity waves observed are 10-12 min and 16-18 min from the power spectra during 14:10-17:30 LT on July 22, 2022. Thus, the height profiles for corresponding dominant periods are extracted and shown in Fig. 13 (b) and (c). Left panels show the amplitude and right panel shows the phase. The maximum amplitudes are observed at 14-16 km for 10-12 min waves, whereas it is at 16-18 km for 16-18 min waves. This indicates there are two sources for these polychromatic waves. The typical property of any atmospheric wave is the propagation of its phase and energy in space and time. The energy will propagate upwards and the phase will propagates downwards, which is clearly observed in the phase profiles of both the waves. These waves can in principle modulate the horizontal stratified layer to form tilting layer as suggested in the earlier studies (e.g. Tsuda et al., 1997b; Muschinski and Wode, 1998; Rao et al., 2008)

4.4 Corrections for non-turbulent factor of spectral width

The observed spectral width is actually a combination of both turbulent and non-turbulent contributions as mentioned above. Thus, it is important to understand and quantify the contribution due to non-turbulent factors such as beam-broadening, wind shear, other transient effects and gravity waves. Although the effect of beam-broadening and wind shear have been studied separately it has been seen that simply adding them up from a 1D model case is not sufficient for actual 2D/3D cases (Nastrom, 1997). The simple yet effective model developed by Nastrom (1997) under very ideal assumptions such as constant wind speed and wind shear under 2D model actually deviate from the real radar case. This has been addressed by the model proposed by Deghghan and Hocking (2011) for a 3D case (D-H model) with some more modifications to fit real wind profile which encapsulates the singular contribution due to the two factors and their

396 combined effect as well. This has been successfully used in studies related to real radars
397 (e.g., Chen et al. 2022). Ignoring transient and gravity wave related broadening effects
398 due to their diminutive contributions with respect to the other factors, the observed
399 spectral width can be defined as:

400 $$\sigma_o{}^2 = \sigma_t{}^2 + \sigma_{s\&b}{}^2 \quad (7)$$

401 Where $\sigma_t{}^2$ is the turbulent part and $\sigma_{s\&b}{}^2$ the contribution due to shear and beam
402 broadening is given by the D-H model as:

403 $$\sigma_{s\&b}{}^2 = \frac{\theta^2}{k} v^2 cos^2\chi - a_0 \frac{\theta}{k} sin\chi \left(v \frac{\partial v}{\partial z}\zeta\right) + b_0 \frac{2sin^2\chi}{8k} \left(\frac{\partial v}{\partial z}\zeta\right)^2 + c_0(cos^2\chi\, sin^2\chi)|v\xi| +$$

404 $$d_0(cos^2\chi\, sin^2\chi)\xi^2 \quad (8)$$

405 Where $k = 4ln2$, $\zeta = 2r\theta sin\chi$, $\xi = \frac{\frac{\partial v}{\partial z}\Delta r}{\sqrt{12}}$, $a_0 = 0.945$, $b_0 = 1.500$, $c_0 = 0.030$, $d_0 = 0.825$

406 and θ is the half power half width, v is the horizontal wind speed, χ is the zenith angle, $\frac{\partial v}{\partial z}$
407 is the vertical shear of horizontal wind, r is the distance from the radar and Δr is the
408 range resolution which is 180 m in the present experiment.

409 Figure 14 shows the (a) wind speed, (b) vertical shear of horizontal winds, observed half-
410 power full spectral width for (c) zenith, and (d) 12 degree off-zenith (East, West, North
411 and South) along with theoretical estimation from D-H model, respectively. This is the
412 case where high wind speed (as high as > 45 ms^{-1}) (Fig. 14 a) and strong wind shear (Fig.
413 14 b) are observed in the UTLS region. The observed turbulence (uncorrected) (Fig. 12 c,
414 d) needs to be corrected for beam broadening for vertical beam and both beam and shear
415 broadening for off-zenith beams. Thus, using D-H model, we estimated the profile for
416 these non-turbulent factors as shown in Fig. 14 (c) and (d) (black square). The model
417 spectral width profiles (non-turbulent factors) above 14 km is exceeding then observed
418 spectral width, thus the effective spectral width will be negative. Although such negative
419 values should not exist theoretically, practically their presence and implication of

420 'negative' energy dissipation rates is addressed by previous studies (Deghghan and
421 Hocking, 2011; Chen et al. 2022). The main reasons for such negative spectral width after
422 correction by non-turbulent factors is due to high wind speed and strong shear
423 contributions. A separate study is planned in near future to address these issue.

424 **4.6 Underestimation of horizontal winds due to aspect sensitivity**

425 One of the consequences of high aspect sensitivity is the underestimation of
426 horizontal winds. The lower the effective beam pointing angle due to high aspect
427 sensitivity, higher will be the underestimation of the horizontal wind. This is quantified
428 by the factor R defined as equation (7) :

429 $$R = 1 + \frac{sin^2 \theta_0}{sin^2 \theta_S} \quad (7)$$

430 The percentage underestimation of horizontal wind given in Fig.15 shows that larger
431 underestimation is observed for layers with higher aspect sensitivity. It can also be seen
432 that the highest underestimation comes for lesser angles such as 6°, 8° with the
433 percentage going as high as 20% or more. While for angles ≥10° the underestimation falls
434 to less than 10% for July 22, 2022 and similar results are also seen for July 21, 2022 as
435 shown in Figure S10. Previous studies for 53 MHz radar at Gadanki have also shown
436 similar results (Jain et al., 1997; Das et al., 2022). Thus, it is necessary to correct the
437 horizontal wind velocities by taking aspect sensitivity into consideration to get correct
438 information regarding the prevalent winds.

439 **5. Concluding remarks**

440 In the present study, aspects sensitivity characteristics for CUSAT ST-radar
441 operating at 205 MHz are assessed for the first time. An experiment was designed to
442 obtain the full volume imaging of the radar backscattering echoes to show the presence
443 of anisotropic and isotropic layers during the Indian summer monsoon. The present

study revealed that the volume scanning of the radar can provide a better understanding of the underlying plausible mechanisms for the occurrence of turbulence, and aspect sensitivity characteristics. Different parameters associated with aspect sensitivity characteristics are also estimated from the CUSAT ST-radar. Aspect sensitivity is found to be present in layers mostly above 12 km height up to the tropopause level which was well detected as a stable stratified layer from the analysis of SNR, spectral width, and Richardson number. The important role that atmospheric stability and wind shear can play in generating anisotropic scattering for aspect sensitive signals is highlighted in the present analyses. The possible presence of tilting layers can be inferred from the strong off zenith enhancement of SNR which can be attributed to possible Kelvin-Helmholtz instability occurring in the height of about 14 km as well as polychromatic gravity waves which can be confirmed from continuous zenith observations. High aspect sensitivity is observed in the vicinity of tropopause and other stratified stable layers, resulting in the underestimation of horizontal winds.

Acknowledgements

The authors are greatly appreciative to the technical and scientific teams of ACARR-CUSAT, Cochin for conducting the experiment and providing the radar data used in this study. The authors also thank the teams of the Ministry of Earth Science (IMD & NCMRWF), UK Met-Office and COSMIC for providing the data used in the study. Authors NP and VV thank the Indian Space Research Organisation (ISRO) for providing a research fellowship during the study period.

Conflict of Interest

The authors declare no conflicts of interest relevant to this study.

Data Availability Statement

The CUSAT ST radar data used for the present study can be downloaded from the website https://spl.gov.in/SPL/images/CUSAT_ST_radar_multibeam. This is a compressed folder (.zip file), which contains all modes of radar data used in the study. Users are requested to obtain permission from Director, ACARR-CUSAT and authors for using the CUSAT ST radar data for any scientific studies. COSMIC-2, radiosonde, IMDAA reanalysis data are publicly available datasets. COSMIC-2 data is available in the website https://data.cosmic.ucar.edu/gnss-ro/cosmic2/nrt/level2. Radiosonde data are available from the University of Wyoming sounding data archive http://weather.uwyo.edu/upperair/sounding.html. IMDAA reanalysis data can be downloaded from https://rds.ncmrwf.gov.in/ upon registration.

References

Anandan, V. K., Rao, I. S., & Reddy, P. N. (2008). A study on optimum tilt angle for wind estimation using Indian MST radar. *Journal of Atmospheric and Oceanic Technology*, *25*(9), 1579-1589. doi: 10.1175/2008JTECHA1030.1.

Ashrit, R., Rani, S.I., Kumar, S., Karunasagar, S., Arulalan, T., Francis, T., Routray, A.,Laskar, S.I., Mahmood, S., Jermey, P., Maycock, A., Renshaw, R., George, J.P., Rajagopal, E.N. (2020). IMDAA regional reanalysis: performance evaluation during

Indian summer monsoon season. *Journal of Geophysical Research-Atmosphere*, 125 (2), e2019JD030973 https://doi.org/10.1029/2019JD030973.

Chen, Z., Tian, Y., & Lü, D. (2022). Turbulence Parameters in the Troposphere—Lower Stratosphere Observed by Beijing MST Radar. *Remote Sensing*, 14(4), 947. https://doi.org/10.3390/rs14040947

Damle, S. H., Chakravarty, T., Kulkarni, A., & Balamuralidhar, P. (1994). Aspect sensitivity measurements of backscatter with ST mode of the Indian MST radar. *Indian Journal of*

494 *Radio and Space Physics, 23*, 67–70.
495 https://nopr.niscpr.res.in/handle/123456789/35844.
496 Das, S. S., Patra, A. K., & Narayana Rao, D. (2008). VHF radar echoes in the vicinity of
497 tropopause during the passage of tropical cyclone: First observations from the
498 Gadanki MST radar. *Journal of Geophysical Research: Atmospheres*, *113*(D9). doi:
499 10.1029/2007JD009014.
500 Das, S. S., K. K. Kumar, K. N. Uma, M. V. Ratnam, A. K. Patra, S. K. Das, A. K. Ghosh, et al.
501 (2014). Modulation of Thermal Structure in the Upper Troposphere and Lower
502 Stratosphere (UTLS) Region by Inertia Gravity Waves: A Case Study Inferred from
503 Simultaneous MST Radar and GPS Sonde Observations. *Indian Journal of Radio and*
504 *Space Physics 43* (1), 11–23. http://nopr.niscair.res.in/handle/123456789/27168 .
505 Das, S. S., Venkat Ratnam, M., Uma, K. N., Patra, A. K., Subrahmanyam, K. V., Girach, I. A.,
506 Suneeth, K. V., et al. (2016). Stratospheric intrusion into the troposphere during the
507 tropical cyclone Nilam (2012). *Quarterly Journal of the Royal Meteorological*
508 *Society*, *142*(698), 2168-2179. doi: 10.1002/qj.2810.
509 Das, S. S., Ratnam, M. V., Rao, M. D., & Uma, K. N. (2022). Volume imaging of aspect
510 sensitivity in VHF radar backscatters: first results inferred from the Advanced Indian
511 MST radar (AIR). *International Journal of Remote Sensing*, *43*(12), 4517-4540. doi:
512 10.1080/01431161.2022.2111667.
513 Dehghan, A., & Hocking, W. K. (2011). Instrumental errors in spectral-width turbulence
514 measurements by radars. *Journal of atmospheric and solar-terrestrial physics*, 73(9),
515 1052-1068. https://doi.org/10.1016/j.jastp.2010.11.011
516 Gage, K. S. (1990). Radar observations of the free atmosphere: Structure and dynamics.
517 In *Radar in Meteorology: Battan Memorial and 40th Anniversary Radar Meteorology*

518 *Conference*, 534-565. Boston, MA: American Meteorological Society. doi:10.1007/978-
519 1-935704-15-7_37
520 Gage, K. S., & Balsley, B. B. (1980). On the scattering and reflection mechanisms
521 contributing to clear air radar echoes from the troposphere, stratosphere, and
522 mesosphere. *Radio Science*, *15*(2), 243-257. doi: 10.1029/RS015i002p00243.
523 Ghosh, A. K., Das, S. S., Patra, A. K., Rao, D. N., & Jain, A. R. (2004). Aspect sensitivity in the
524 VHF radar backscatters studied using simultaneous observations of Gadanki MST
525 radar and GPS sonde. *Annales Geophysicae*, *22*(11),4013-4023. Göttingen, Germany:
526 Copernicus Publications. doi: 10.5194/angeo-22-4013-2004.
527 Hocking, W. K. (1985). Measurement of turbulent energy dissipation rates in the middle
528 atmosphere by radar techniques: A review. *Radio Science*, 20(6), 1403-1422.
529 doi:10.1029/RS020i006p01403
530 Hocking, W. K. (1989). "Target Parameter Estimation." In *MAP Handbook*, edited by S.
531 Fukao, 228–268. Vol. 30. SCOSTEP Secr., Univ of Ill. *Urbana*.
532 Hocking, W. K., Rüster, R., & Czechowsky, P. (1986). Absolute reflectivities and aspect
533 sensitivities of VHF radio wave scatterers measured with the SOUSY radar. *Journal of*
534 *atmospheric and terrestrial physics*, *48*(2), 131-144, doi:10.1016/0021-
535 9169(86)90077-2.
536 Hocking, W. K., Fukao, S., Tsuda, T., Yamamoto, M., Sato, T., & Kato, S. (1990). Aspect
537 sensitivity of stratospheric VHF radio wave scatterers, particularly above 15-km
538 altitude. *Radio Science*, *25*(4), 613-627. doi: 10.1029/RS025i004p00613
539 Jain, A. R., Rao, Y. J., & Rao, P. B. (1997). Aspect sensitivity of the received radar backscatter
540 at VHF: Preliminary observations using the Indian MST radar. *Radio Science*, *32*(3),
541 1249-1260. doi: 10.1029/97RS00252.

Mohanakumar, K., Kottayil, A., Anandan, V. K., Samson, T., Thomas, L., Satheesan, K., Rebello, R. et al. (2017). Technical details of a novel wind profiler radar at 205 MHz. *Journal of Atmospheric and Oceanic Technology*, *34*(12), 2659-2671. doi: 10.1175/JTECH-D-17-0051.1.

Muschinski, A., & Wode, C. (1998). First in situ evidence for coexisting submeter temperature and humidity sheets in the lower free troposphere. *Journal of the Atmospheric Sciences*, *55*(18), 2893-2906. doi:10.1175/1520 - 0469(1998)055<2893:FISEFC>2.0.CO;2.

Nastrom, G. D. (1997). Doppler radar spectral width broadening due to beamwidth and wind shear. *Annales Geophysicae*, 15(6), 786-796. Springer-Verlag. https://doi.org/10.1007/s00585-997-0786-7

Qing, H., Zhao, Z., Xu, Y., & Zhou, C. (2018). Observation and study of the aspect sensitivity and echo mechanism based on the Wuhan MST radar. *IEEE Geoscience and Remote Sensing Letters*, 16(2), 211-215. doi:10.1109/LGRS.2018.2871824.

Rao, D. N., Kishore, P., Rao, T. N., Rao, S. V. B., Reddy, K. K., Yarraiah, M., & Hareesh, M. (1997). Studies on refractivity structure constant, eddy dissipation rate, and momentum flux at a tropical latitude. *Radio Science*, *32*(4), 1375-1389. doi: 10.1029/97RS00251.

Rao, T. N., Uma, K. N., Rao, D. N., & Fukao, S. (2008). Understanding the transportation process of tropospheric air entering the stratosphere from direct vertical air motion measurements over Gadanki and Kototabang. *Geophysical Research Letters*, *35*(15). https://doi.org/10.1029/2008GL034220

Rani, S.I., Arulalan, T., George, J.P., Rajagopal, E.N., Renshaw, R., Maycock, A., Barker, D.M., Rajeevan, M. (2021). IMDAA: high-resolution satellite-era reanalysis for the Indian

monsoon region. *Journal of Climate*. 34 (12), 5109–5133. https://doi.org/10.1175/JCLI-D-20-0412.1.

Röttger, J., & Liu, C. H. (1978). Partial reflection and scattering of VHF radar signals from the clear atmosphere. *Geophysical Research Letters*, *5*(5), 357-360. doi: 10.1029/GL005i005p00357.

Samson, T. K., Kottayil, A., Manoj, M. G., Babu, B., Rakesh, V., Rebello, R., et al. (2016). Technical aspects of 205 MHz VHF mini wind profiler radar for tropospheric probing. *IEEE Geoscience and Remote Sensing Letters*, 13(7), 1027–1031. https://doi.org/10.1109/lgrs.2016.2561965.

Tsuda, T., VanZandt, T. E., & Saito, H. (1997a). Zenith-angle dependence of VHF specular reflection echoes in the lower atmosphere. *Journal of Atmospheric and Solar-Terrestrial Physics*, *59*(7), 761-775. doi: 10.1016/S1364-6826(96)00057-0.

Tsuda, T., Gordon, W. E., & Saito, H. (1997b). Azimuth angle variations of specular reflection echoes in the lower atmosphere observed with the MU radar. *Journal of Atmospheric and Solar-Terrestrial Physics*, *59*(7), 777-784. doi: 10.1016/S1364-6826(96)00058-2.

Veenus, V., Das, S. S., Sama, B., and Uma, K. N. (2022), A comparison of temperature and relative humidity measurements derived from COSMIC-2 radio occultations with radiosonde observations made over the Asian summer monsoon region, *Remote Sensing Letters*, 13 (4), 394–405, doi:10.1080/2150704X.2022.2033345.

Worthington, R. M. (1999). Calculating the azimuth of mountain waves, using the effect of tilted fine-scale stable layers on VHF radar echoes. *Annales Geophysicae*, *17*(2), 257-272. Göttingen, Germany: Springer Verlag. doi: 10.1007/s00585-999-0257-4.

589 Worthington, R. M. (2005). VHF volume-imaging radar observation of aspect-sensitive
590 scatterers tilted in mountain waves above a convective boundary layer. In *Annales*
591 *Geophysicae* ,*23*(4), 1139-1145. doi:10.5194/angeo-23-1139-2005.
592 Worthington, R. M., & Thomas, L. (1997). Long-period unstable gravity-waves and
593 associated VHF radar echoes. *Annales Geophysicae*,*15*(6), 813-822. Berlin/Heidelberg:
594 Springer-Verlag. doi: 10.1007/s00585-997-0813-8.
595 Worthington, R. M., Palmer, R. D., & Fukao, S. (1999). An investigation of tilted aspect-
596 sensitive scatterers in the lower atmosphere using the MU and Aberystwyth VHF
597 radars. *Radio Science*, *34*(2), 413-426. doi: 10.1029/1998RS900028.

598
599

600 **Figure captions**

601 **Figure 1.** Beam configurations for different modes of experiment. See Table 2 for details.

602 **Figure 2.** (a) Wind speed and direction (arrow) at 100 hPa, and (b) outgoing-long wave
603 radiation along with mean sea level pressure at 13:30 LT on July 21 (left) and 22 (right),
604 2022. CUSAT ST radar is marked in each panels.

605 **Figure 3.** Fan sector maps in the E-W and N-S directions for (a) Signal-to-Noise (SNR),
606 (b) Doppler velocity values, (c) uncorrected observed half-power full Spectral width at
607 13:30 LT on July 22, 2022.

608 **Figure 4.** SNR as a function of zenith angles up to 30° in East-West (left) and North-South
609 (right) directions for heights of 11.4 km, 12.4 km, 14 km and 16.4 km for July 22, 2022

610 **Figure 5.** Doppler spectra as a function of zenith angle for July 22, 2022 for East-West
611 (left) and North-South (right) planes.

612 **Figure 6.** Volume scan slices at 14 km, 16 km and 17.6 km for (a) SNR, (b) Doppler, (c)
613 uncorrected half-power full spectral width at 12 LT on July 22, 2022.

Figure 7. Altitude profiles of SNR difference between zenith and a few off-zenith angles for East, West, North, and South directions.

Figure 8. Aspect Angle θs (top) and Horizontal correlation length ζ (bottom) for off-zenith angles up to 20˚ with respect to the zenith beam for East, West North, and South directions. Black dotted lines in the top and bottom panels correspond to the threshold values of 3.093˚ and 7.187 m for aspect angle and correlation length for the radar.

Figure 9. Effective beam pointing angle (θ_{eff}) for off-zenith angles.

Figure 10. Scatter plots of aspect sensitivity parameter ($SNR_{Zenith\text{-}Oblique}$) against (a) wind shear (b) stability for East-West (top) and North-South (bottom) for July 22, 2022.

Figure 11. Height-time intensity plots of (a) SNR, (b) vertical velocity (w) and (c) uncorrected half-power full spectral width for continuous zenith observations starting at 14:10:23 LT on July 22, 2022.

Figure 12. Altitude profiles of (a) zonal and meridional winds derived from the radar, (b) temperature obtained from COSMIC-2 satellite for (9.63˚N, 76.12˚E), (c) Stability, (d) wind Shear and (e) Richardson Number at 13:16:07 LT on July 22, 2022.

Figure 13. (a) Power spectra of vertical velocity at 14.8 and 15.7 km, height profiles of amplitude (left) and phase (right) for (b) 10-12 min, and (c) 16-18 min dominant periods during 14:10-17:30 LT on July 22, 2022.

Figure 14. Height profiles of (a) horizontal wind speed (U_h), (b) vertical shear (S) of U_h, (c) observed spectral width (σ^2)vertical beam (red) along with theoretical estimation for beam-broadening (black squares), and (d) observed spectral width in East (solid blue), West (dash blue), North (solid green), South (dash green) for 12 degree off-zenith along with DH model by considering both beam and shear broadening on July 22, 2022.

Figure 15. Altitude profiles of percentage of underestimating factor of horizontal wind (R) on July 22, 2022.

Table captions

Table 1. Radar parameters of CUSAT ST Radar as used for the experiment.

Table 2. Beam configuration and sequence of scan azimuth and zenith scan angles for the four modes. Values in parentheses denote azimuth and zenith angle with (0,10) signifying North 10° tilt and the azimuthal angles follow the meteorological convention with (90,10),(180,0) and (270,0) as East 10°, South 10° and West 10° respectively.

Figure 1. Beam configurations for different modes of experiment. See Table 2 for details.

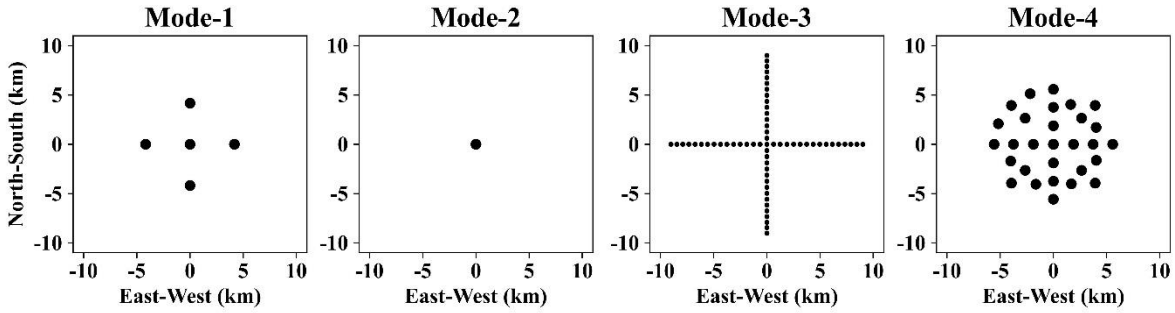

Figure 2. (a) Wind speed and direction (arrow) at 100 hPa, and (b) outgoing-long wave radiation along with mean sea level pressure at 13:30 LT on July 21 (left) and 22 (right), 2022. CUSAT ST radar is marked in each panels.

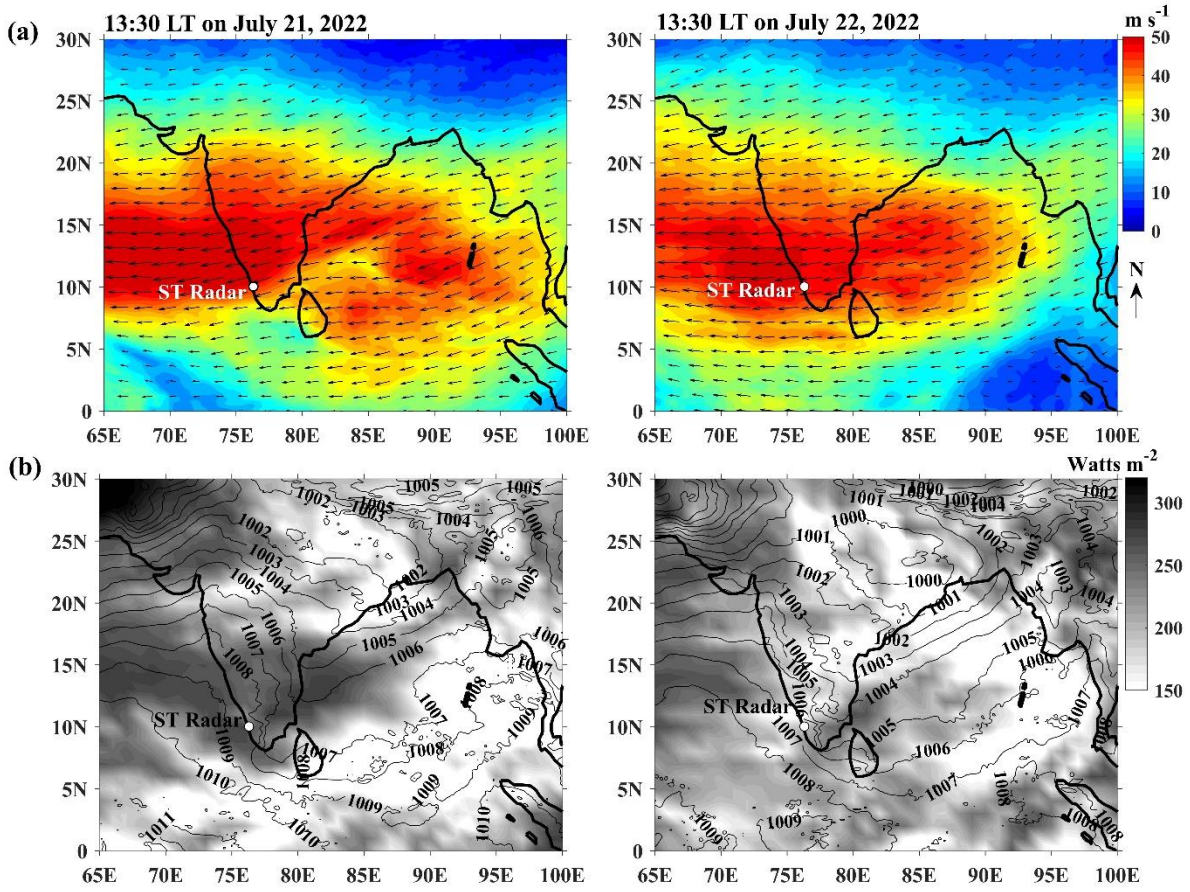

Figure 3. Fan sector maps in the E-W and N-S directions for (a) Signal-to-Noise (SNR), (b) Doppler velocity values, (c) uncorrected observed half-power full Spectral width at 13:30 LT on July 22, 2022.

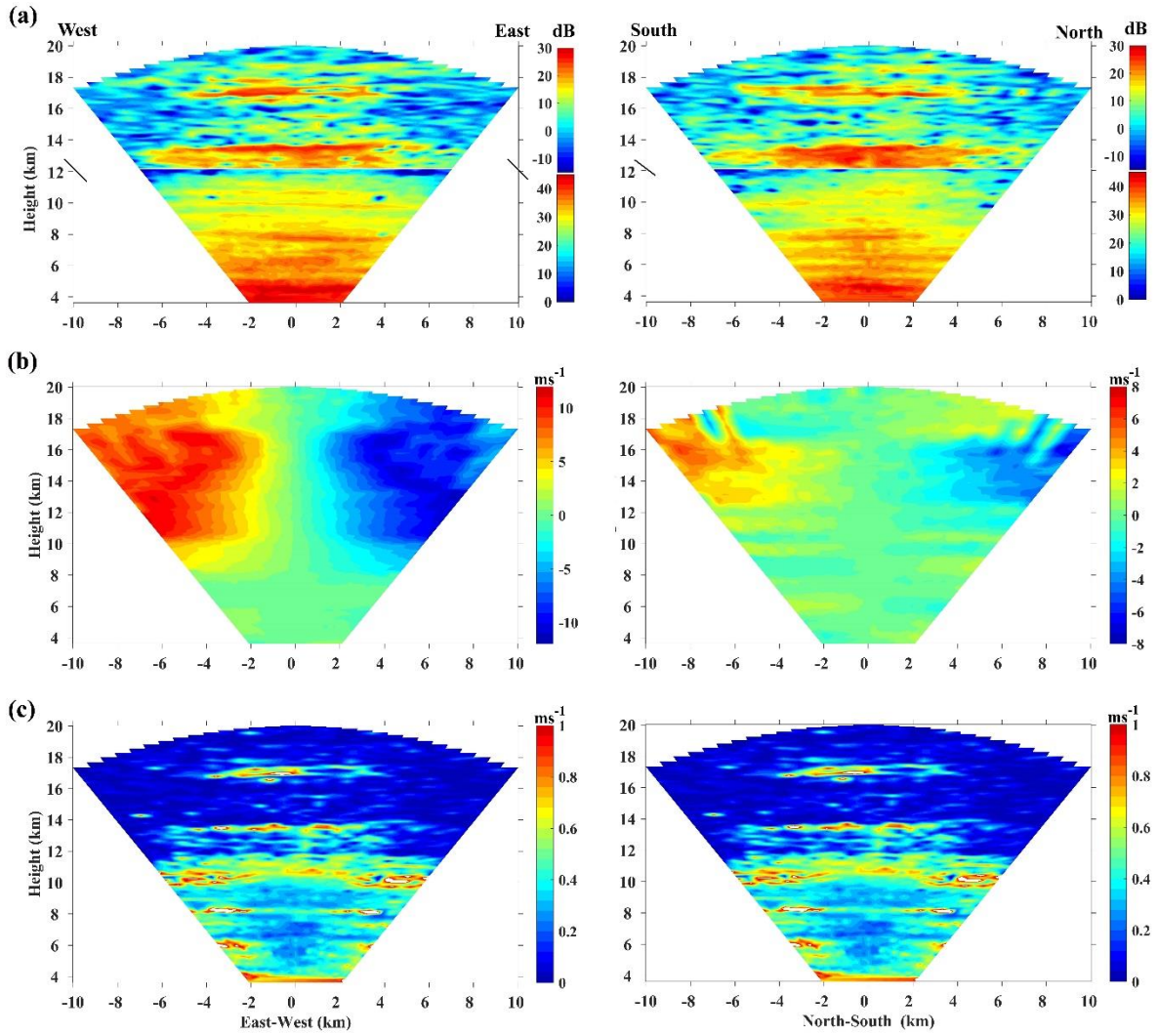

Figure 4. SNR as a function of zenith angles up to 30° in East-West (left) and North-South (right) directions for heights of 11.4 km, 12.4 km, 14 km and 16.4 km for July 22, 2022.

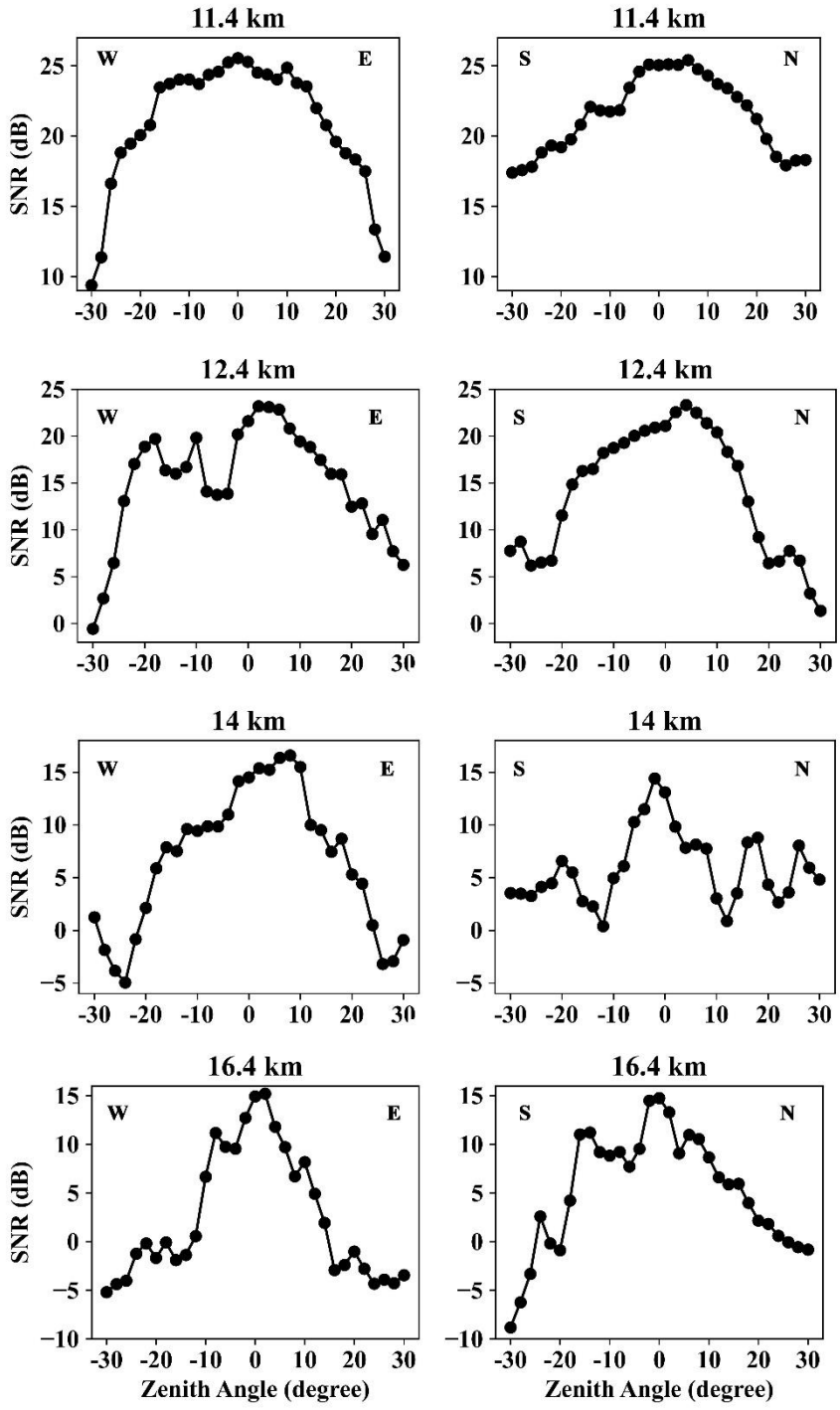

Figure 5. Doppler spectra as a function of zenith angle for July 22, 2022 for East-West (left) and North-South (right) planes.

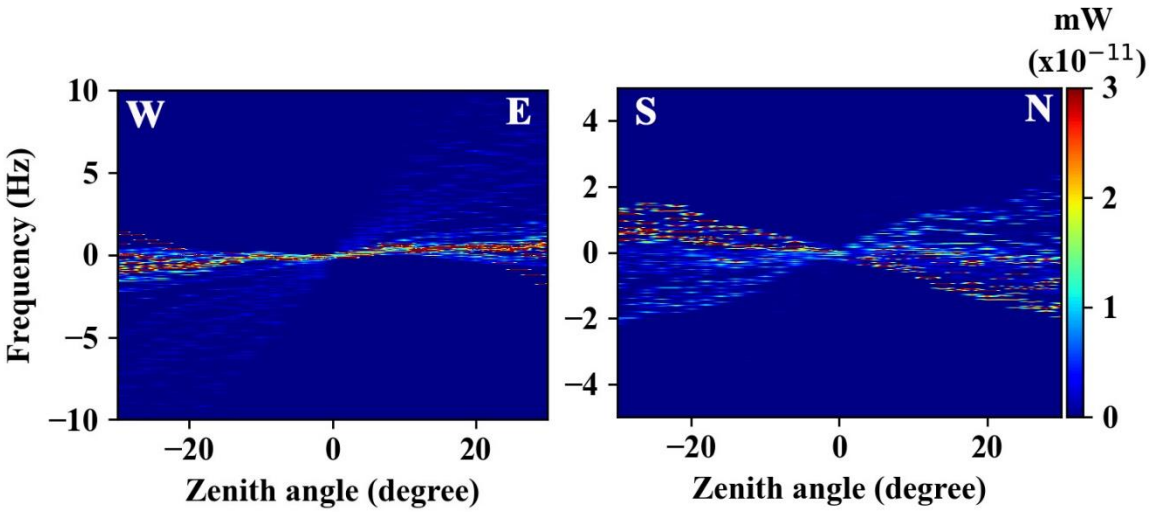

Figure 6. Volume scan slices at 14 km, 16 km and 17.6 km for (a) SNR, (b) Doppler, (c) uncorrected half-power full spectral width at 12 LT on July 22, 2022.

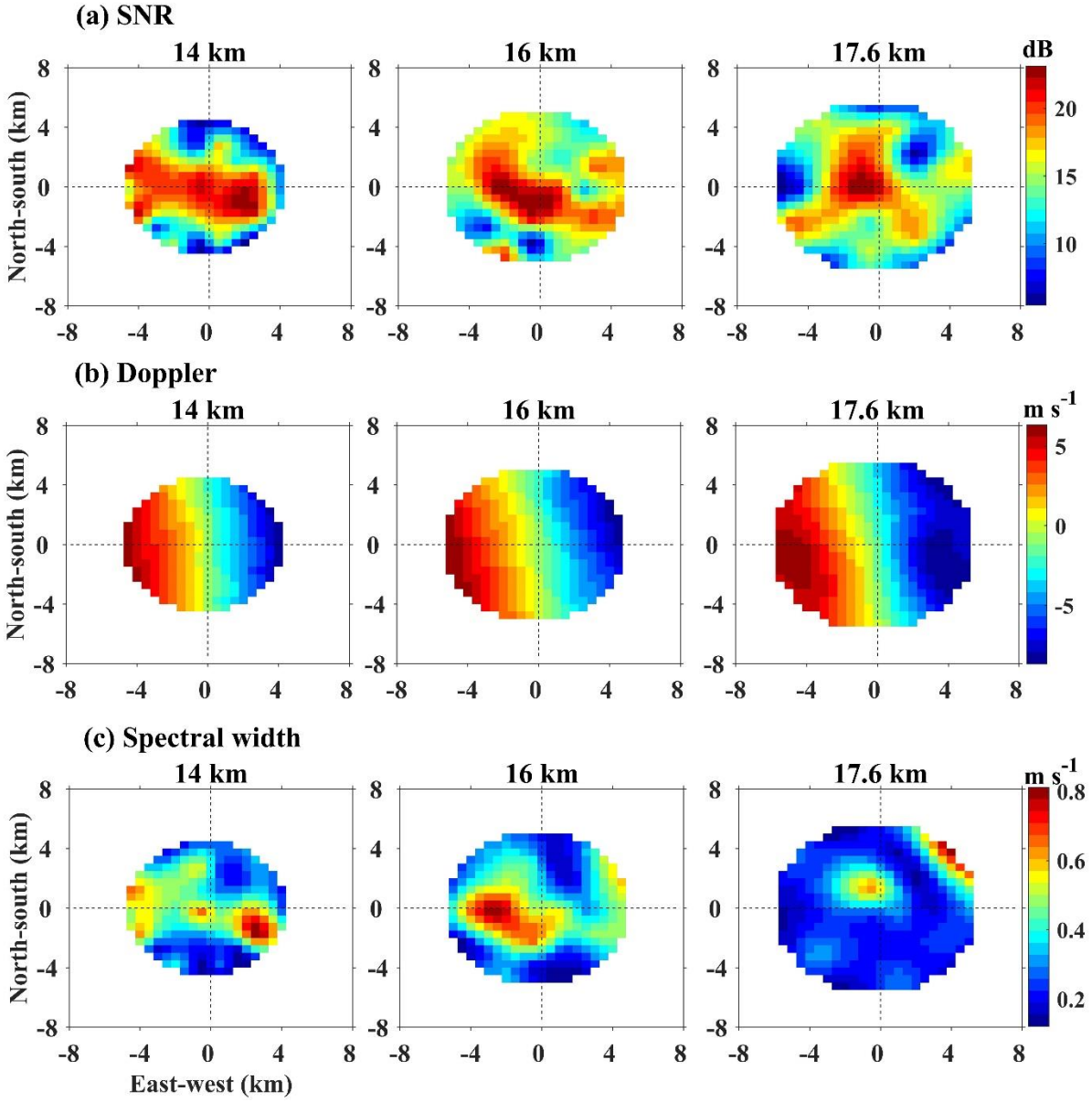

Figure 7. Altitude profiles of SNR difference between zenith and a few off-zenith angles for East, West, North, and South directions.

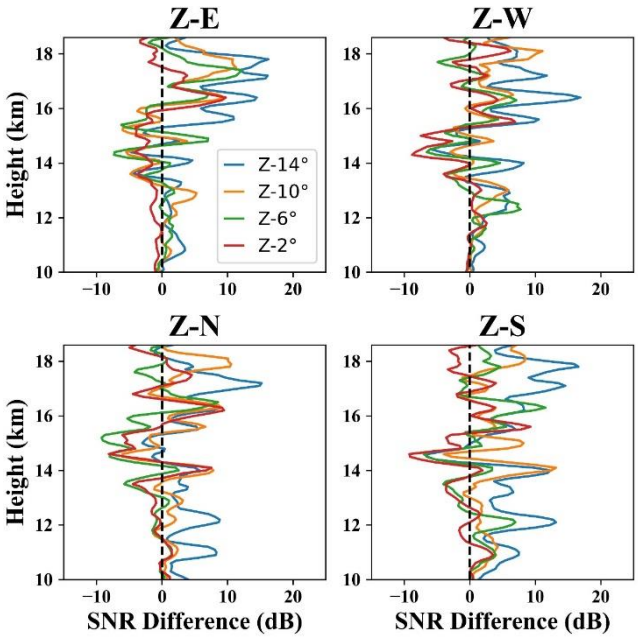

Figure 8. Aspect Angle θs (top) and Horizontal correlation length ζ (bottom) for off-zenith angles up to 20˚ with respect to the zenith beam for East, West North, and South directions. Black dotted lines in the top and bottom panels correspond to the threshold values of 3.093˚ and 7.187 m for aspect angle and correlation length for the radar.

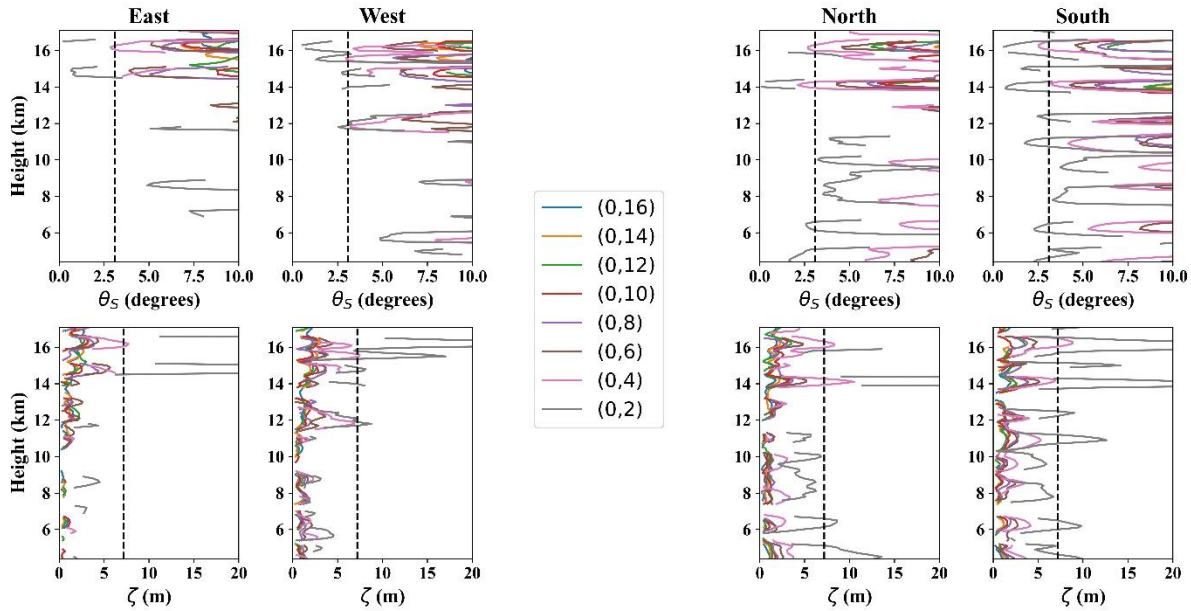

Figure 9. Effective beam pointing angle (θ_{eff}) for off-zenith angles.

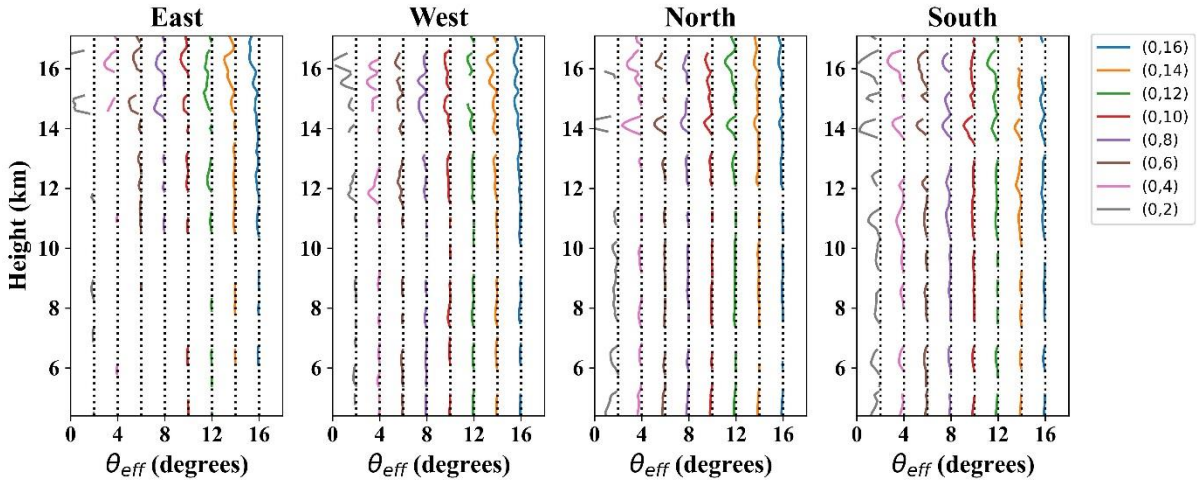

Figure 10. Scatter plots of aspect sensitivity parameter ($SNR_{Zenith\text{-}Oblique}$) against (a) wind shear (b) stability for East-West (top) and North-South (bottom) for July 22, 2022.

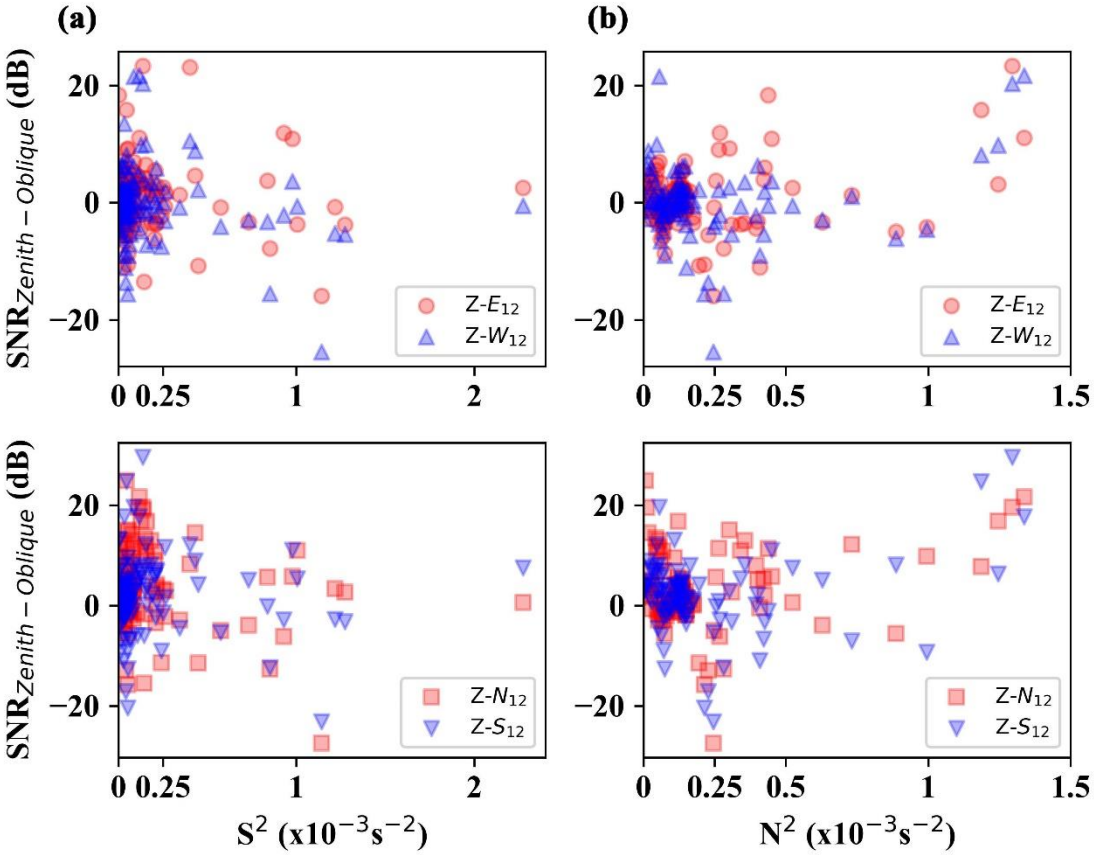

Figure 11. Height-time intensity plots of (a) SNR, (b) vertical velocity (w) and (c) uncorrected half-power full spectral width for continuous zenith observations starting at 14:10:23 LT on July 22, 2022.

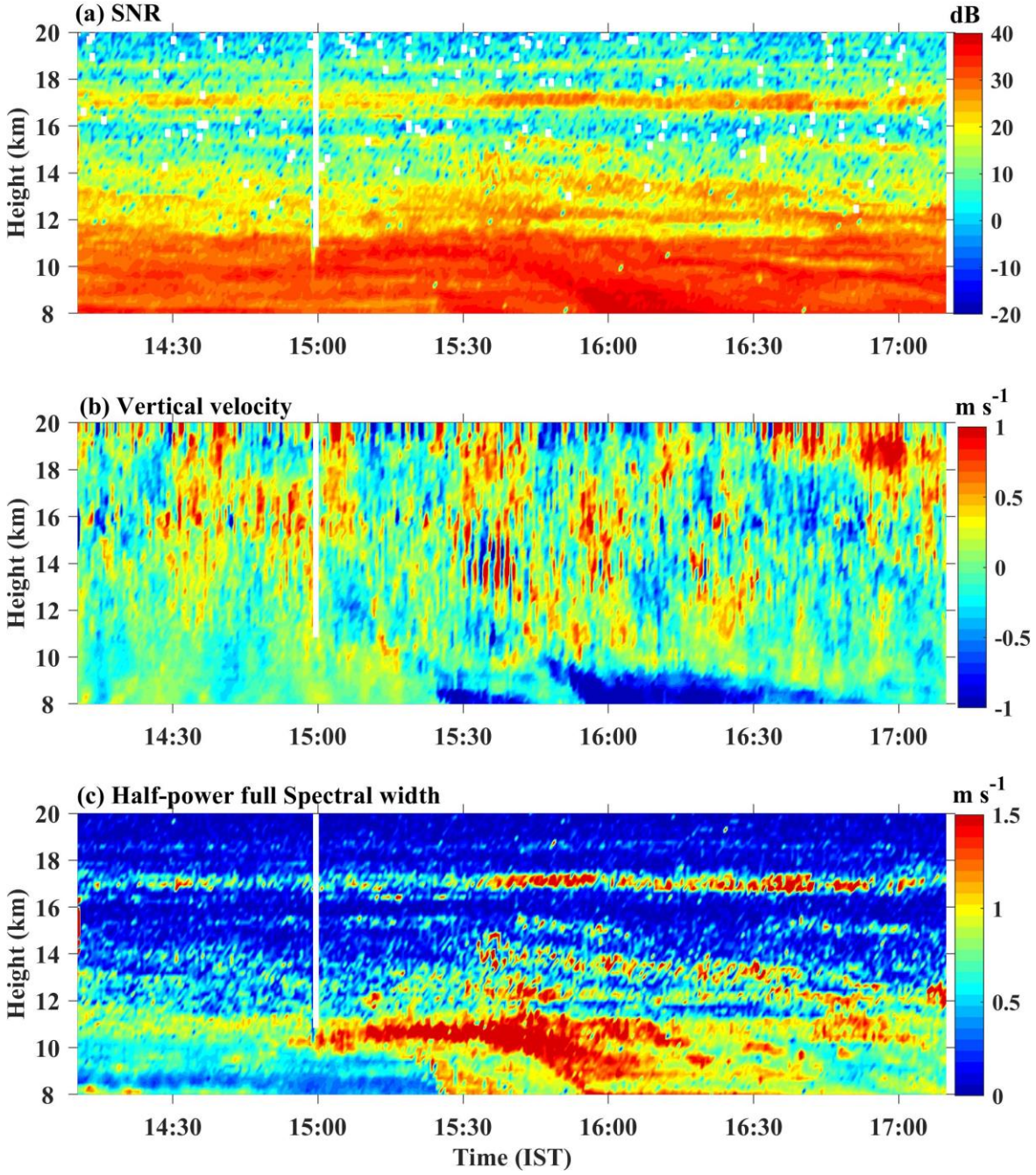

Figure 12. Altitude profiles of (a) zonal and meridional winds derived from the radar, (b) temperature obtained from COSMIC-2 satellite for (9.63°N, 76.12°E), (c) Stability, (d) wind Shear and (e) Richardson Number at 13:16:07 LT on July 22, 2022.

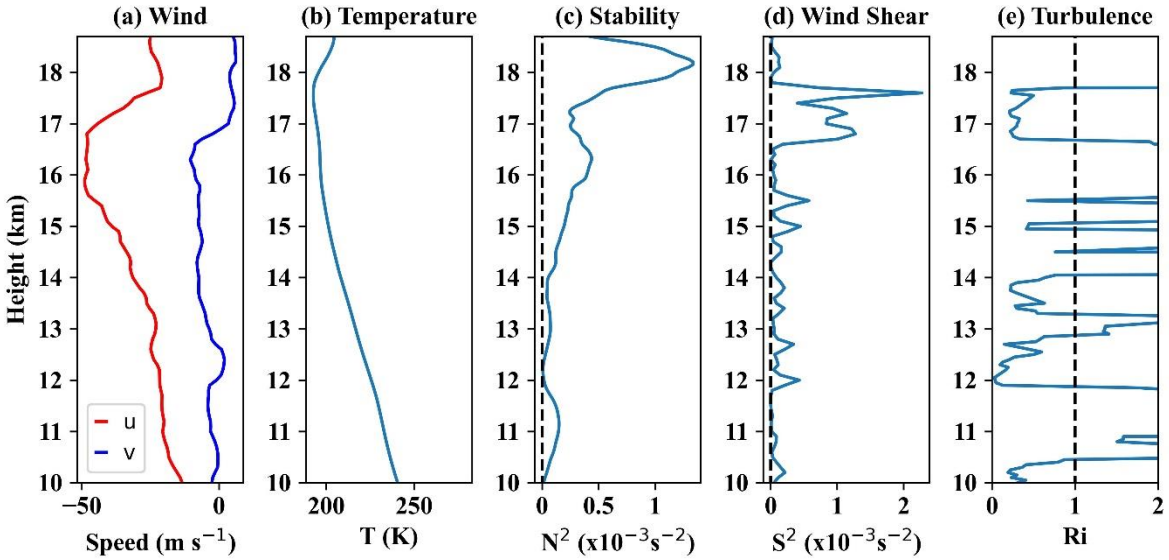

Figure 13. (a) Power spectra of vertical velocity at 14.8 and 15.7 km, height profiles of amplitude (left) and phase (right) for (b) 10-12 min, and (c) 16-18 min dominant periods during 14:10-17:30 LT on July 22, 2022.

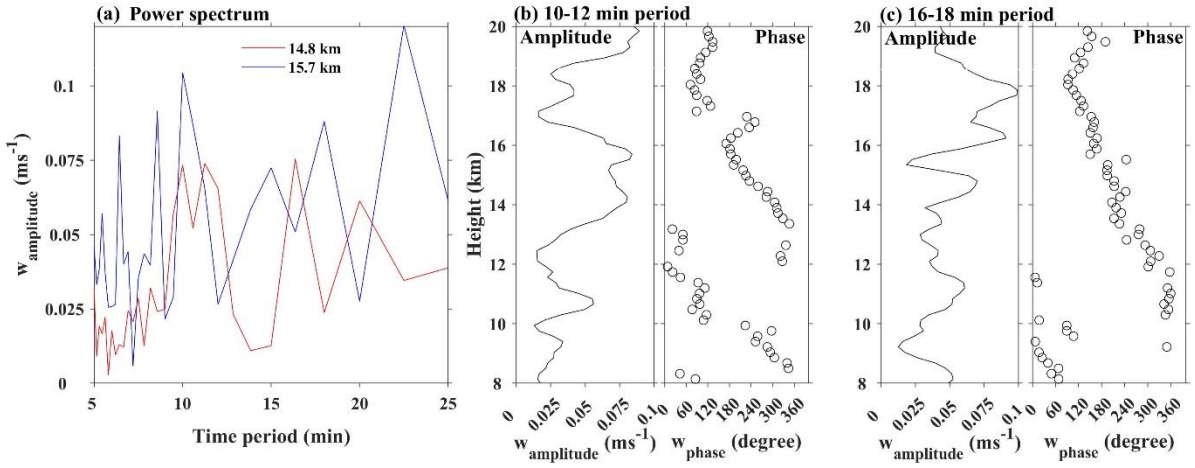

Figure 14. Height profiles of (a) horizontal wind speed (U_h), (b) vertical shear (S) of U_h, (c) observed spectral width (σ^2)vertical beam (red) along with theoretical estimation for beam-broadening (black squares), and (d) observed spectral width in East (solid blue), West (dash blue), North (solid green), South (dash green) for 12 degree off-zenith along with DH model by considering both beam and shear broadening on July 22, 2022.

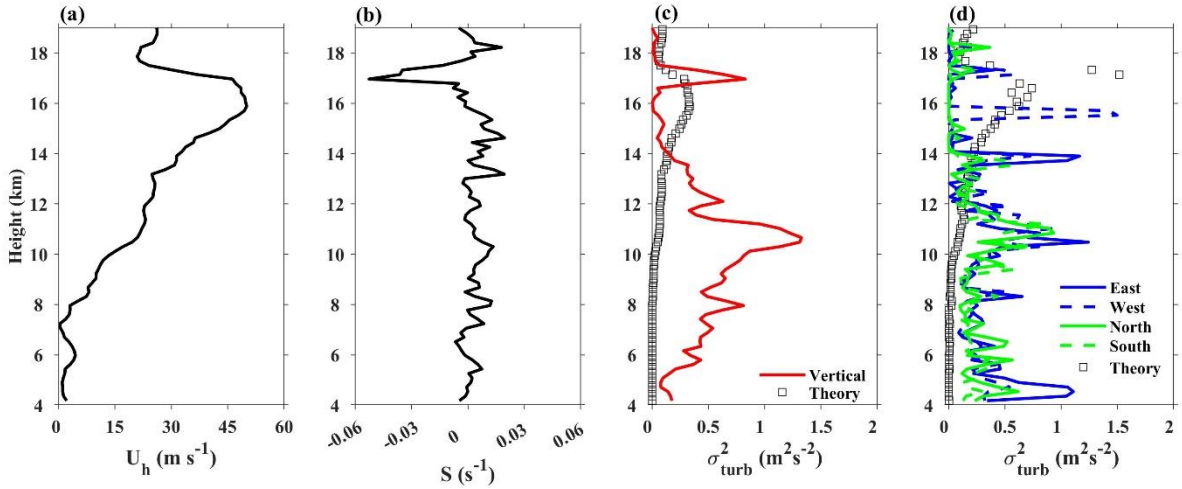

Figure 15. Altitude profiles of percentage of underestimating factor of horizontal wind (R) on July 22, 2022

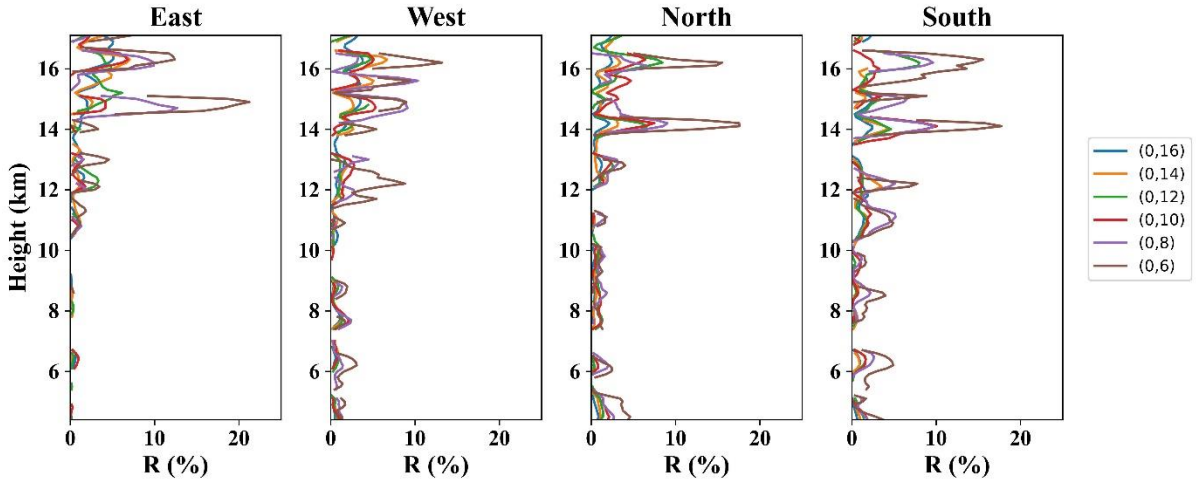

Table 1. Radar parameters of CUSAT ST Radar as used for the experiment.

Parameter	**Value**
Frequency	205MHz
Antenna	619 - 3 Element Yagi Uda Antenna
Mode of operation	Doppler Beam Swinging (DBS)
Peak Transmitted power	309 kW (TRM Peak power- 500 W)
Transmitted type	BPSK Modulation
Beam width	3°
Effective area	536 m^2
Peak Power aperture product	~1.6 x10^8 Wm^2
Duty cycle	11.9%
Pulse width	19.2 μs
Inter Pulse Period (IPP)	161.29 μs
Pulse Code	Complementary/ Barker code
Range Resolution	180 m
No. of FFT points	1024
No. of Coherent Integrations	128
No. of Incoherent integrations	1
No. of Beams	31 / 61
Data format	ASCII

Table 2. Beam configuration and sequence of scan azimuth and zenith scan angles for the four modes. Values in parentheses denote azimuth and zenith angle with (0,10) signifying North 10° tilt and the azimuthal angles follow the meteorological convention with (90,10),(180,0) and (270,0) as East 10°, South 10° and West 10° respectively.

Mode	**Mode 1**	**Mode 2**	**Mode 3**	**Mode 4**
Date	21 and 22 July 2022	22 July 2022	21 and 22 July 2022	21 and 22 July 2022
Time (LT)	Day 1- 12:17:26-12:20:26 Day 2- 12:48:38-12:51:38	14:10:23-17:10:23	Day 1- 13:32:48-14:46:00 Day 2- 13:01:36-14:14:48	Day 1- 12:10:45-12:47:57 Day 2- 11:39:32-12:16:44
No. of Scans	2	6	2	2
Azimuth and Zenith angles	(90,12),(0,0), (270,12), (0,12),(180,12)	All (0,0)	(90,30),(90,28),…, (90,4),(90,2), (0,0),(270,2),(270,4),…,(270,28),(270,30), (0,30)(0,28),…,(0,4), (0,2),(180,2),(180,4),…,(180,28),(180,30)	(0,0),(0,6),(90,6),(180,6), (270,6),(0,0),(0,12),(45,12), (90,12),(135,12),(180,12), (225,12),(270,12),(315,12), (0,0),(0,18),(22,14),(45,18), (67,14),(90,18),(112,14), (135,18),(157,14),(180,18), (202,14),(225,18),(247,14), (270,18),(292,18),(315,18), (337,18)
No. of beams	5	50	61	31

Structures and backscattering characteristics of CUSAT 205 MHz Stratosphere-Troposphere Radar at Cochin (10.04^{o}N, 76.3^{o}E) - First results

Nabarun Poddar[1,2], Siddarth Shankar Das[1,*], Veenus Venugopal[1,2], S. Abhilash[3] , V. Rakesh[3]

[1]Space Physics Laboratory, Vikram Sarabhai Space Centre, Thiruvananthapuram-695022
[2]Department of Physics, University of Kerala, Thiruvananthapuram
[3]Advanced Centre for Atmospheric Radar Research, Cochin University of Science and Technology, Cochin

e-mail: dassiddhu@yahoo.com & siddarth_das@vssc.gov.in

Supplimentry material

Figure S1. Same as Fig.3, but for July 21, 2022.

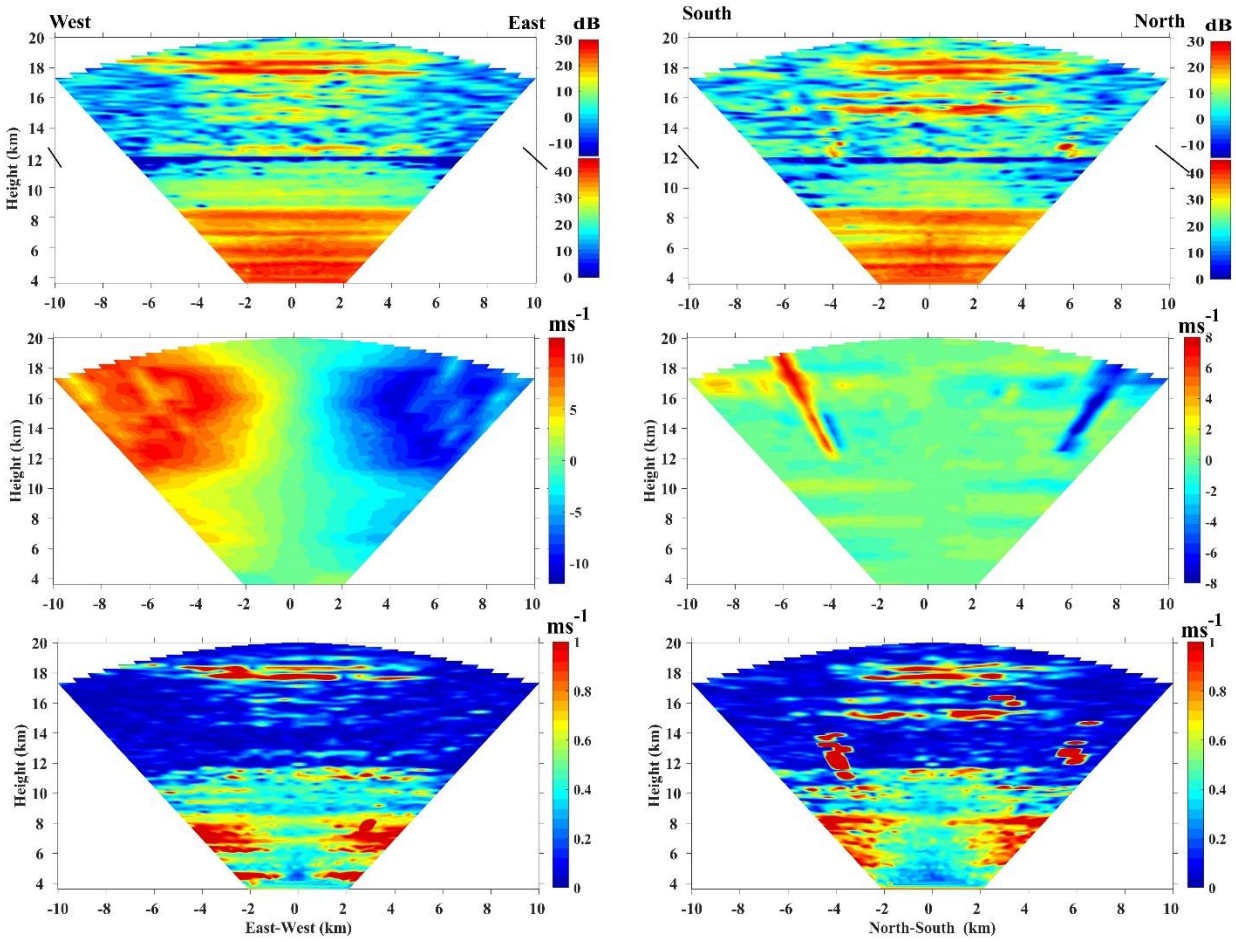

Figure S2. Same as Fig. 4, but for July 21, 2022.

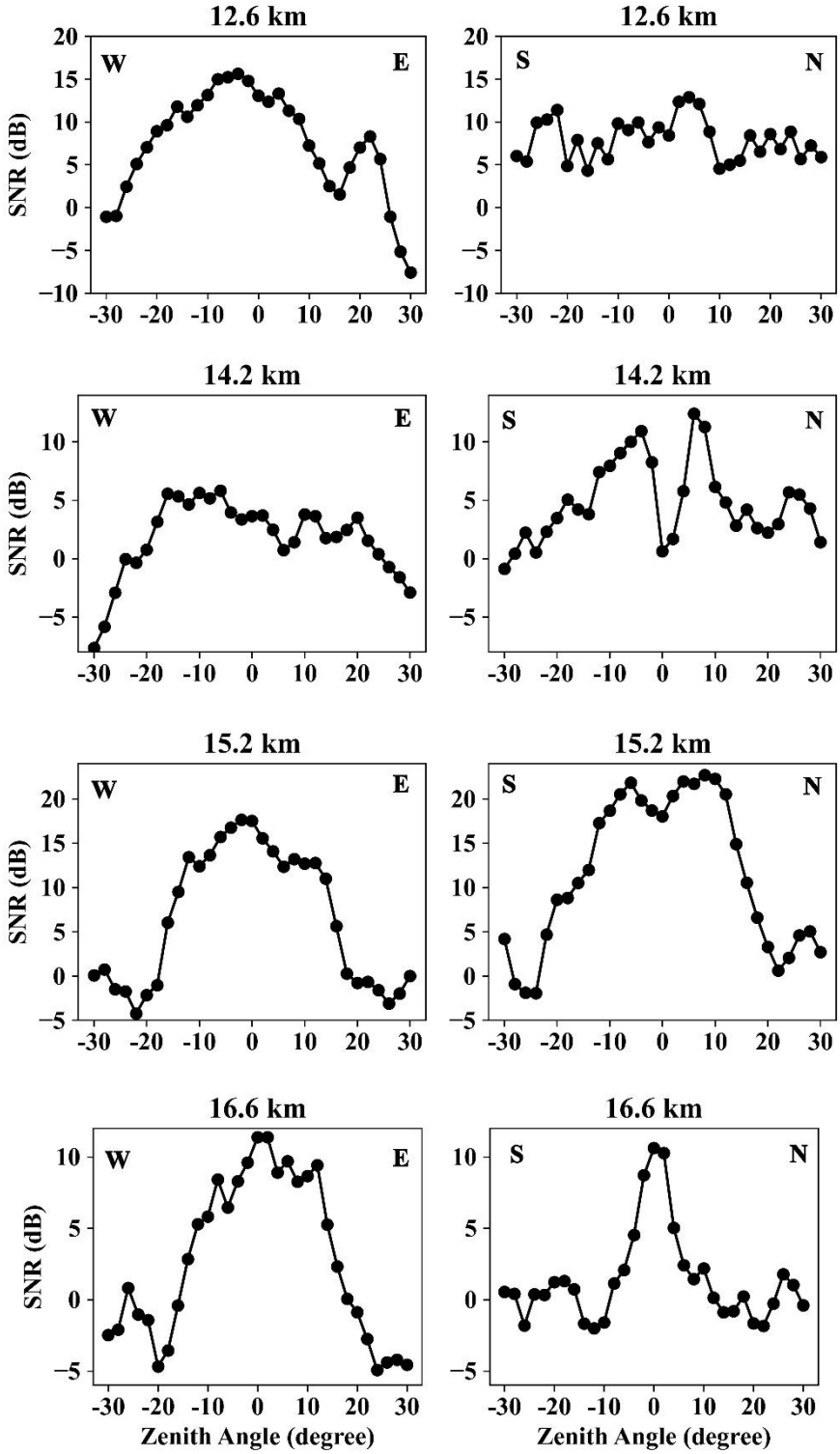

Figure S3. Same as Fig. 5, but for July 21, 2022.

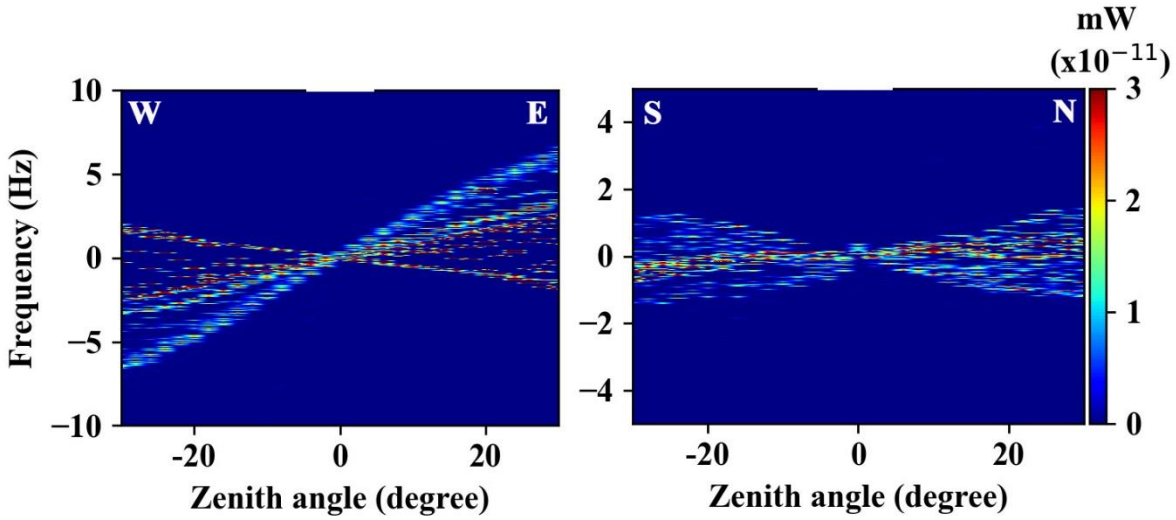

Figure S4. Same as Fig. 6, but for July 21, 2022.

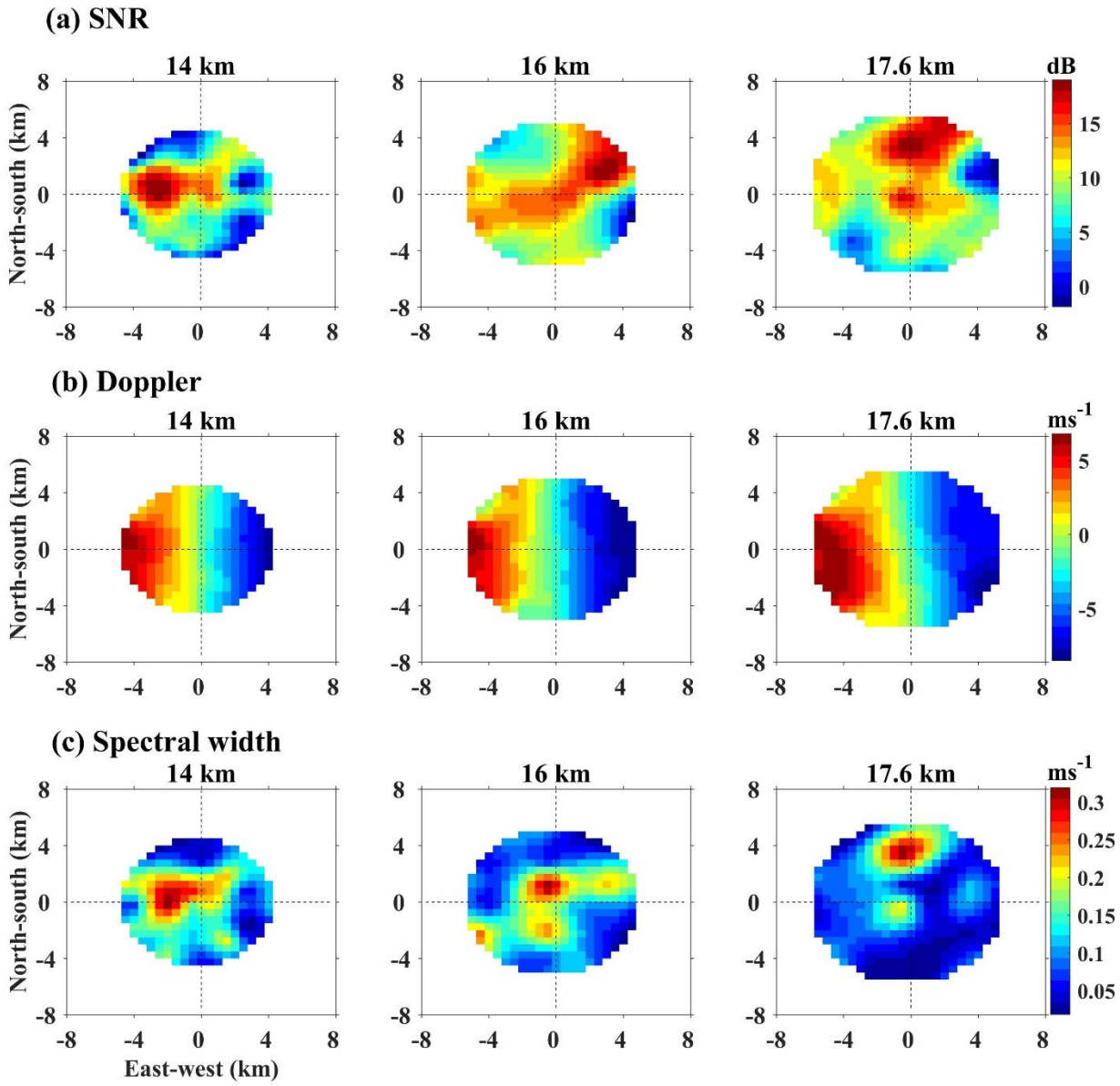

Figure S5. Same as Fig. 7, but for July 21, 2022.

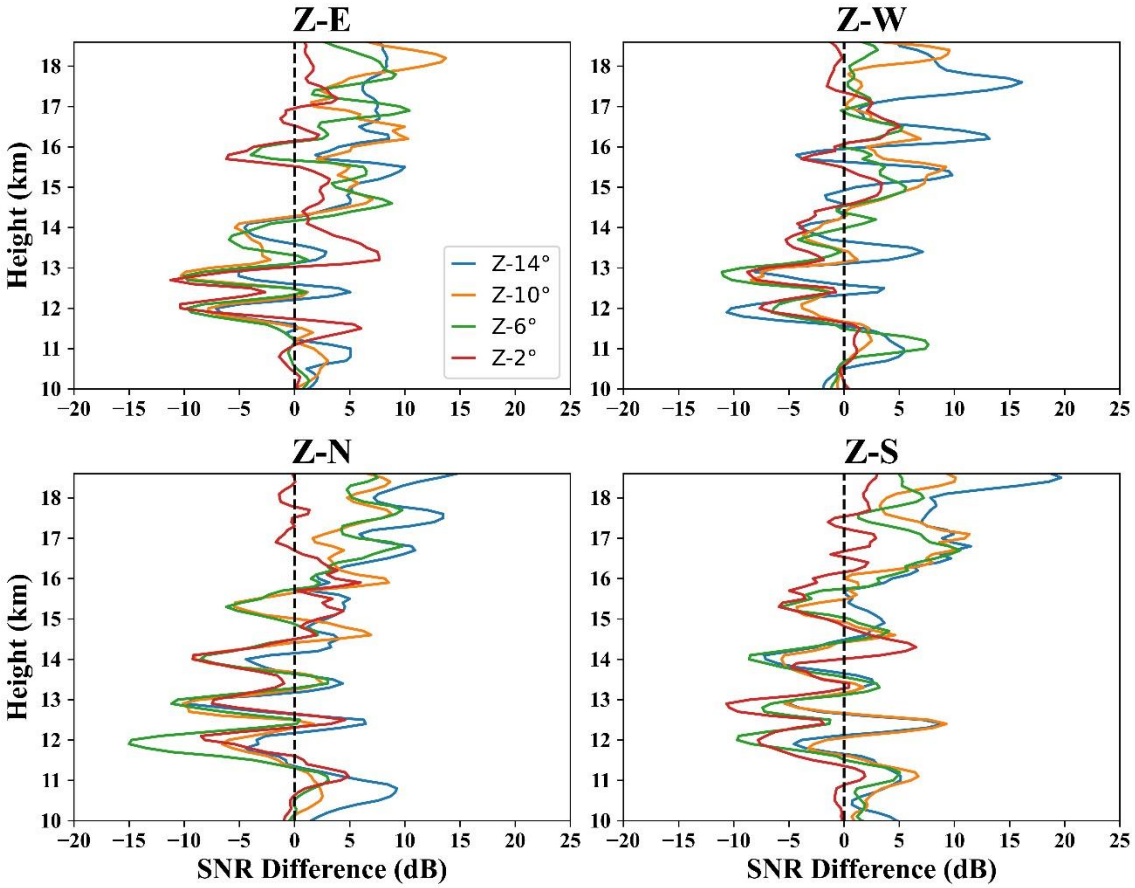

Figure S6. Same as Fig. 8, but for July 21, 2022.

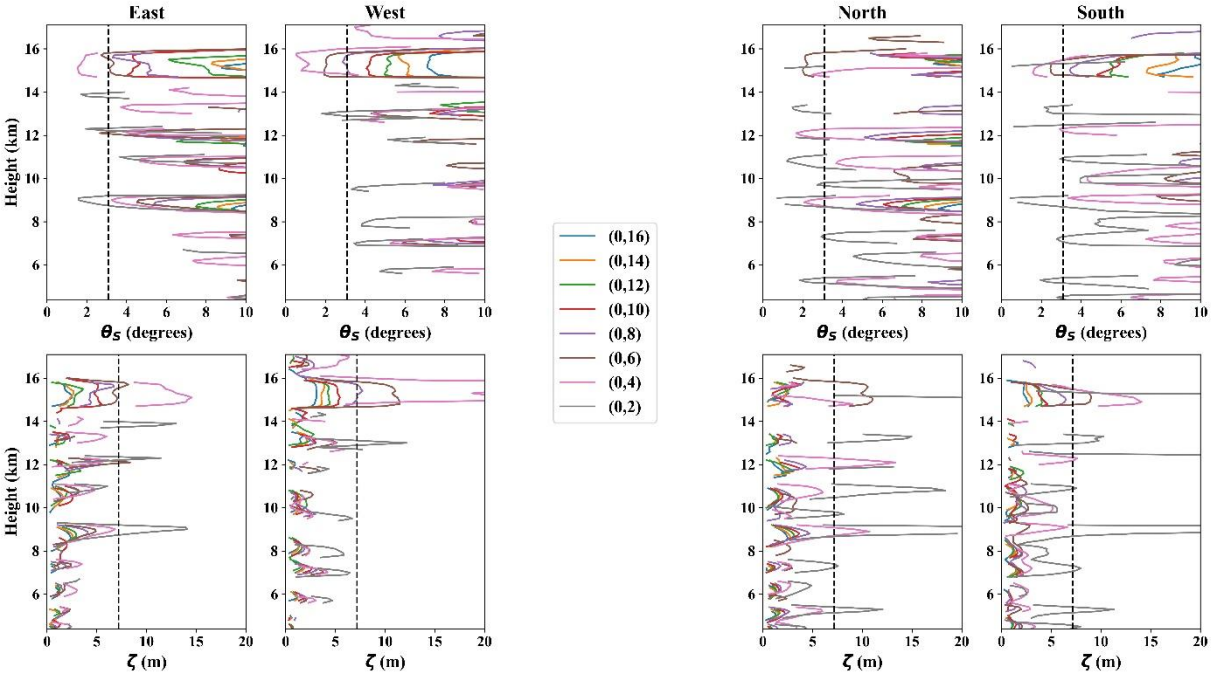

Figure S7. Same as Fig. 9, but for July 21, 2022.

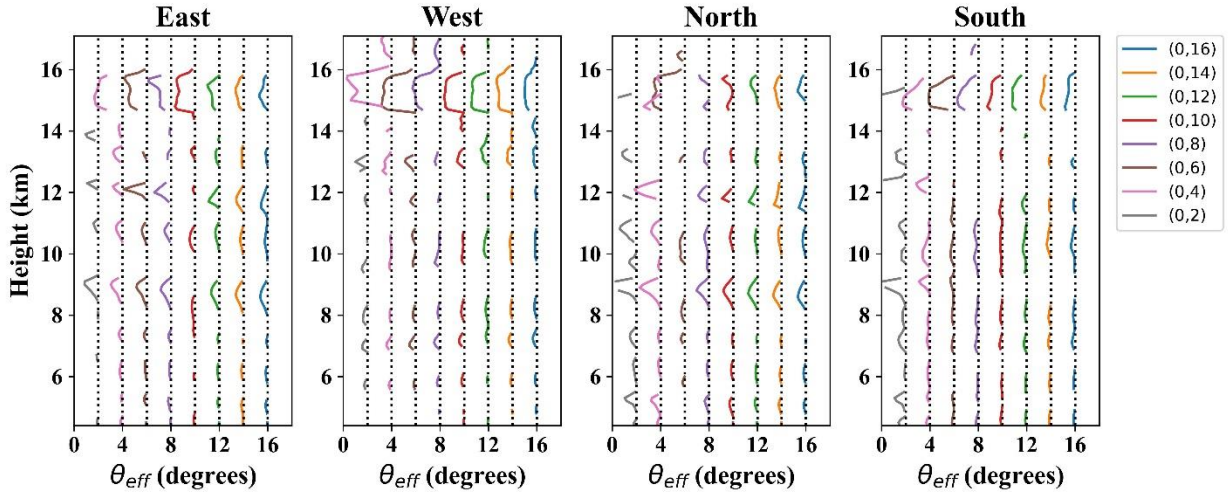

Figure S8. Same as Fig. 10, but for July 21, 2022.

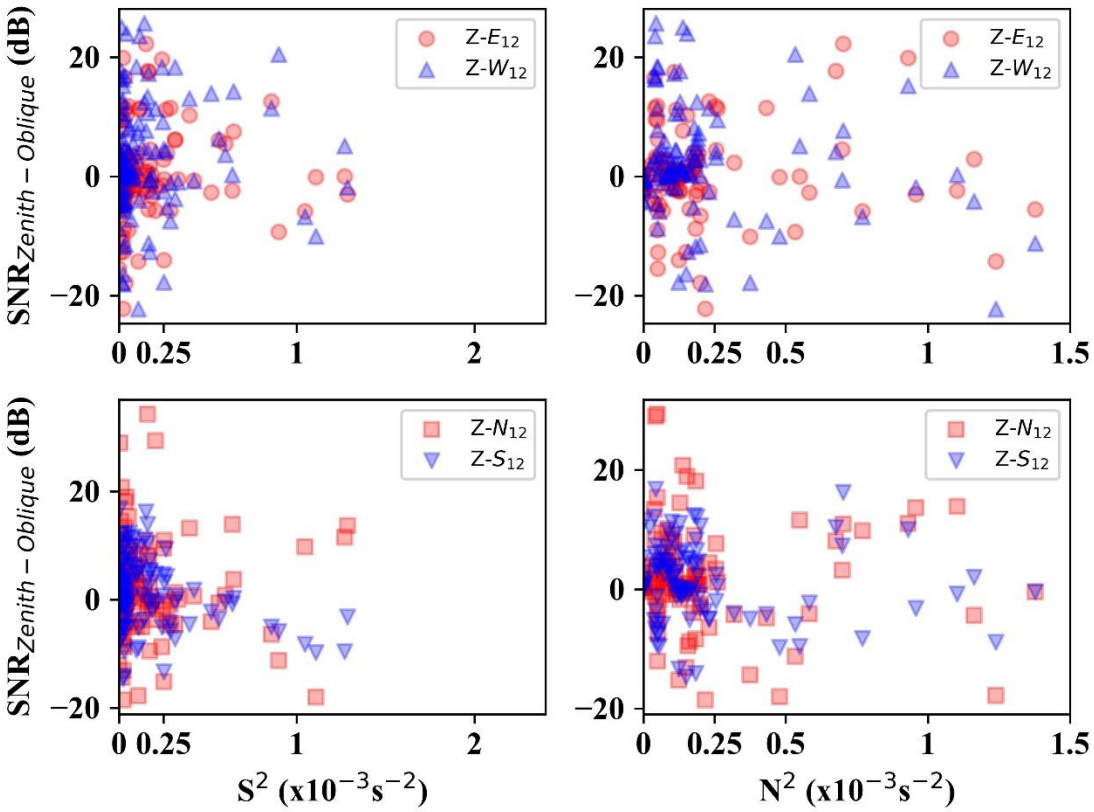

Figure S9. Same as Fig. 12, but for July 21, 2022.

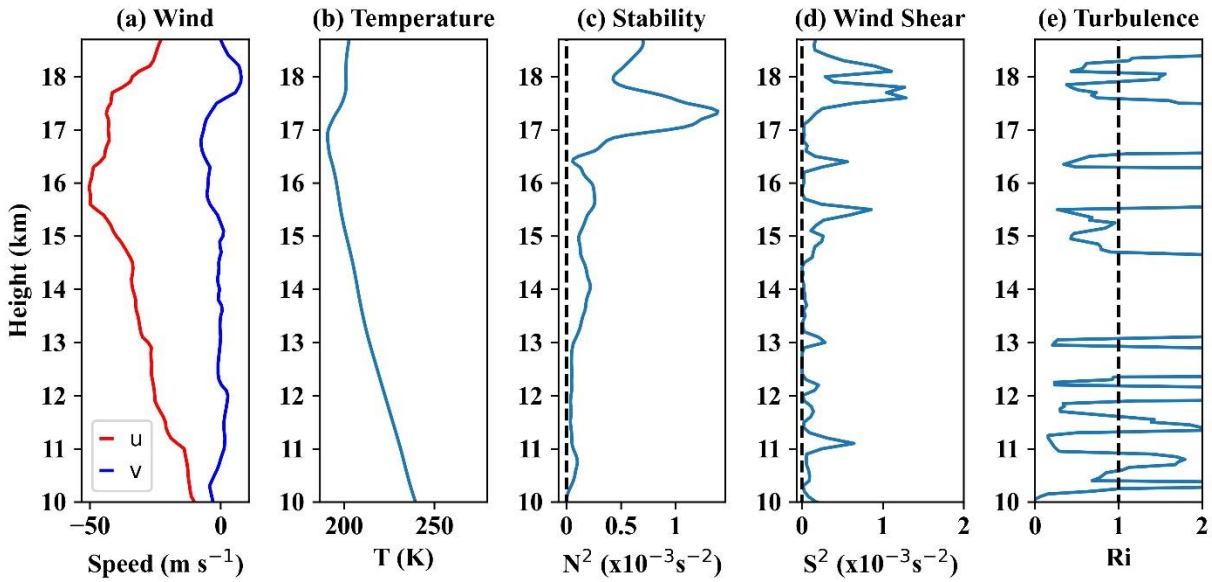

Figure S10. Same as Fig. 15, but for July 21, 2022.